CHARACTERIZING THE INFLUENCE OF LAYERED TRANSITION METAL OXIDE MORPHOLOGY ON CATHODE PERFORMANCE

BY

MICHAEL ANTHONY CAPLE JR.

DISSERTATION

Submitted in partial fulfillment of the requirements
for the degree of Doctor of Philosophy in Materials Science and Engineering
in the Graduate College of the
University of Illinois Urbana-Champaign, 2024

Urbana, Illinois

Doctoral Committee:

Professor Paul V. Braun, Chair
Professor Jessica A. Krogstad
Professor Nenad Miljkovic
Associate Professor Nicola Perry

ABSTRACT

Layered transition metal oxides are an important class of high energy density lithium-ion battery cathode materials. Because of their widespread use, it is important to elucidate factors that influence their stability in secondary battery applications. Using thick (>10 μm), textured lithium cobalt oxide (LCO) cathodes, we reveal the impact of crystallographic orientation on the cycling stability of these layered transition metal oxide materials. We observe that (003) textured (LCO), (104) textured LCO, and composite LCO experience 48.5%, 65.9%, and 67.9% capacity fade after 100 cycles, respectively. Using electrochemical impedance spectroscopy, we measured the half-cell resistance to charge transfer and cathode electrolyte interphase resistance in 20 cycle increments. We detect that the charge transfer resistance grows 2280% for (003) LCO and 755% for (104) LCO, indicating that large regions of the textured cathodes crack during cycling. Conversely, we see that the growth of the cathode electrolyte interphase resistance of composite LCO cathode (95.3%) is much larger than what is observed for the textured LCO cathodes. The subsequent postmortem confocal Raman images confirm that state of charge heterogeneity is present in each cathode; interestingly, the extent of heterogeneity is correlated to the growth of the resistance to charge transfer.

We continued to explore the impact of cathode morphology when studying single crystalline $LiNi_{0.8}Mn_{0.1}Co_{0.1}O_2$, a popular next generation cathode material. Fabrication of single crystals with a low initial cation mixing required optimization of the precursor flux. Using electrochemical impedance spectroscopy, we observed the interfacial changes for single crystals with predominately (012), (001), and (104) surface areas. From the obtained results it is calculated that the charge transfer resistance for (001), (012), and (104) dominant crystals grow

69.4%, 87.1%, and 14.5% in 65 cycles, respectively. Furthermore, we find that the cathode electrolyte interphase resistance for the (104) dominant single crystals only grows 3.82% in 65 cycles while this value grows 31.9% for (012) dominant single crystals in the same cycle range. Overall, the electrochemical results from this study support our assertion that cathodes with a predominately (104) surface area have stable interfacial properties, which make them attractive for long-term cycling. Moreover, our findings indicate that tailoring cathode microstructure is crucial to extending lithium-ion battery cycle life.

ACKNOWLEDGMENTS

I’d first like to acknowledge Dr. Paul Braun for his intellectual and professional support throughout my time as a student in his group. Other students in the group, such as Arghya Patra, Nathan Fritz, Patrick Kwon, Brian Wen, and Hyewon Jeong have been great colleagues for me to have intellectual conversations with. Their help in completing various projects and tasks has been invaluable. I must also acknowledge the support of my colleague Ben Zahiri for his guidance in developing scientific ideas and helping me develop my abilities to communicate my results in a meaningful way. His guidance has been heavily influential in my development as a scientist. I’d be mistaken if I did not take the opportunity to thank Rajen Basu of the Materials Research Lab for his help in completing my studies on nickel rich cathode materials. I believe his help in synthesizing cathodes was important in shortening the lead time to obtain meaningful results in this study.

Throughout my dissertation, several friends and family have been present to support me. My best friends, Connor Mahan, Garrett Simkins, and Jonathan Rodriguez have been there for me during this time, and I cannot thank them enough for doing so. My sisters, Nina, Camryn, and Kiona have embraced my direction as being the first member in the family to complete this level of education. Our conversations on the significance of this achievement for our family have kept me driven throughout the challenges that I confronted during this process. Lastly, I’d like to thank my parents, Michael Caple Sr., Jennifer Caple, and Salina Roby for the encouragement and helping me become the person I am today. They help me strive to not be stagnant in who I am and support me in pushing my creative boundaries.

This dissertation is dedicated to my late grandmother Janet Berry for her passion for education and her push for me completing my degree. Although you are not here with us physically, I have always continued to keep you in my thoughts during this challenge.

TABLE OF CONTENTS

LIST OF ABBREVIATIONS

CA	Chronoamptometry
CEI	Cathode-Electrolyte Interphase
CRS	Confocal Raman Spectroscopy
CV	Cyclic voltammetry
DMC	Dimethyl Carbonate
EC	Ethylene Carbonate
EIS	Electrochemical impedance spectroscopy
GITT	Galvanostatic Intermittent Titration Technique
ICP-MS	Inductively Coupled Plasma Mass Spectrometry
LCO	Lithium Cobalt Oxide
LIB	Lithium-Ion Battery
NMC	Lithium Nickel Manganese Oxide
SEI	Solid-Electrolyte Interphase
SEM	Scanning Electron Microscopy
XRD	X-Ray Diffraction

CHAPTER 1: INTRODUCTION

1.1 Lithium-Ion Batteries

Over the last 30 years, lithium-ion batteries (LIBs) have become ubiquitous in technologies ranging from portable electronics to electric vehicles.[1] This popularity is due to the fact that LIBs have the highest combination of gravimetric energy density (Wh/kg) and volumetric energy density (Wh/L) in comparison to other battery technologies. As a result, there has been a considerable research thrust to further develop LIB technology.[2] A general schematic of a LIB is depicted in Fig. 1., where the flow of electrons in the external circuit is balanced by lithium-ion flow between the anode and cathode of a LIB. The working principle of a LIB can be described by coupled electrochemical processes between the anode and cathode.[3] These processes are described by two different steps. During charge, an external voltage source lowers the voltage of the anode, which induces electron flow to the anode through the external circuit and lithium-ion flow to the anode through the electrolyte; the anode undergoes reduction. Concurrently, the voltage of the cathode is raised, which provides the lithium-ions for this process. Moreover, the anode and cathode undergo reduction and oxidation during charge, respectively. During discharge, lithium-ion flow from the anode to the cathode provides current to power an external load (e.g. a cell phone). The redox reactions that occur during this step are reversed to what occurs during the charge process. It is imperative to note that, for liquid electrolytes, a polymeric based separator must be included to physically isolate the anode and cathode, which prevents shorting of the cell from occurring.

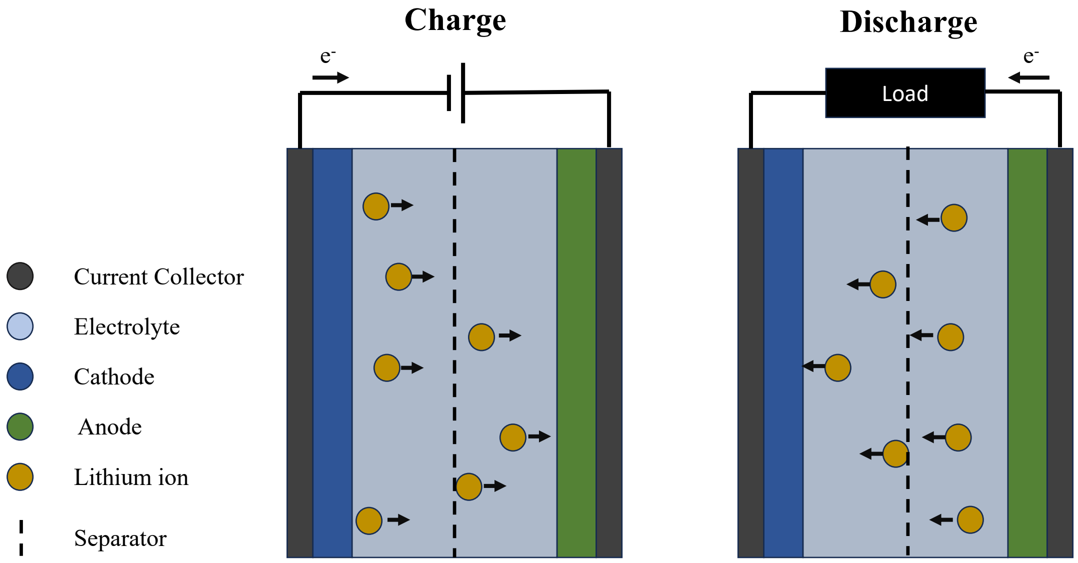

Figure 1.1: Schematic of a generic lithium-ion battery. The function of this cell is described by charge (left) and discharge (right). As indicated, transfer of electrons in the external circuit is supported by transfer of Li-ions across the cell.

As each electrode acts as hosts for the lithium-ions during LIB operation, the anode and cathode have been a significant subject of LIB research. Although the anode is a significant focus of research itself, the cathode is the focus of this thesis as it acts a limit on the total capacity of the LIB.[4] This is because, generally, current cathode active materials have limitations in structural stability that prevents researchers from extracting their total capacity. As a result, the focus of improving cathodes has included tailoring cathode morphology, tuning the transition metal site of popular cathode materials, and coating the surface of cathode materials. The latter two categories are significant for extending the cycle life of the synthesized cathode material, but understanding the implications of cathode morphology on LIB cycle life are critical to maximizing the potential cycle life of these materials.

1.2 Lithium Transition Metal Oxides for Lithium-Ion Batteries

The active materials used for LIB cathodes are categorized by the crystal structure of the active material. The most popular cathode materials include olivines ($LiFePO_4$, LFP), spinels (e.g. $LiMn_2O_4$, LMO), and layered transition metal oxides (LTMOs, e.g. $LiCoO_2$, LCO).[5] A summary of popular choices for cathode materials are summarized in Fig. 1.2, where the gravimetric (specific energy, Wh/kg) and volumetric energy density (energy density, Wh/L) of each cathode is compared.[6] Each class of cathode material has advantageous properties that drive their commercial popularity; however, LTMOs (e.g. NCM 811, LCO, NCA) have received particular attention in LIB research field due to their superior gravimetric and volumetric capacity compared to other cathode materials. In addition, these materials are popular for their high operating voltage and low manufacturing cost.[7]

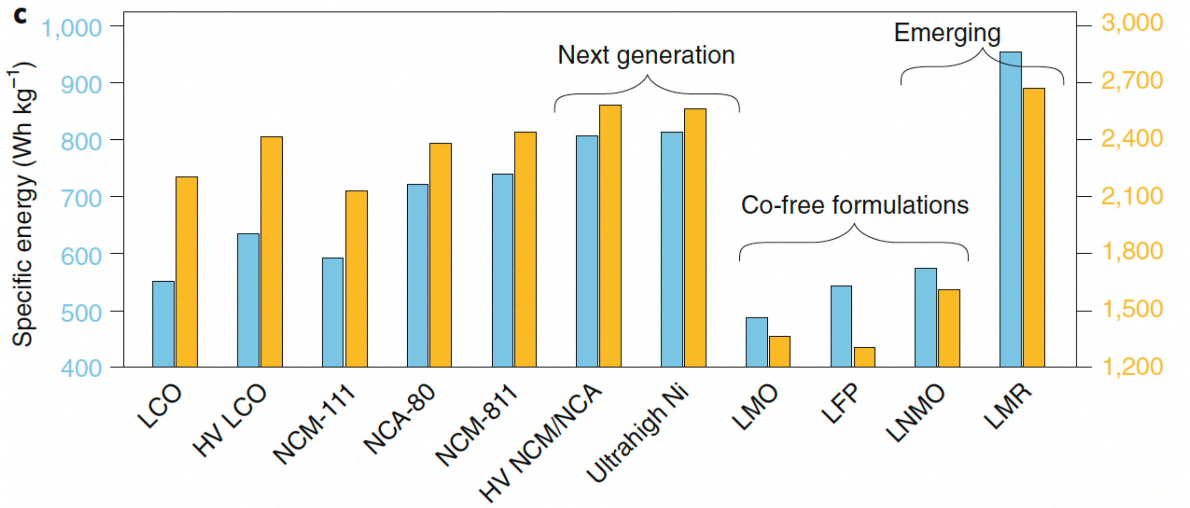

Figure 1.2: Popular cathode materials for LIBs are compared by their specific energy and energy density (Reproduced from [6]).

A schematic of an LTMO crystal is shown in Fig. 1.3. As their name suggests, the LTMOs materials are defined by repeating stacks of lithium layers and TMO_2 layers.[5] Despite their advantages, the limited structural stability of these materials at high voltages limits their practically achievable capacity.[8] To improve their electrochemical characteristics, a major research thrust for LTMO cathodes has been manipulating the anisotropic properties of these materials to improve their structural stability, which will concurrently improve their long-term cyclability at high voltage and/or high-rate operation. It is also imperative to note that modifying the transition metal site by doping the active material and modifying the surface chemistry of these materials with more inert coatings are strategies to further improve their cyclability.[9], [10], [11], [12]

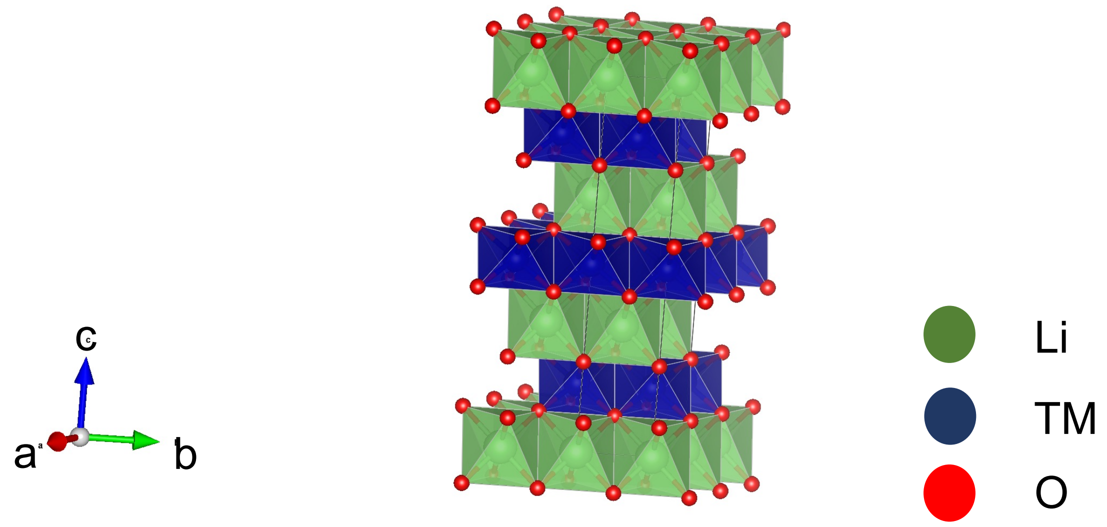

Figure 1.3: Schematic of a Layered Transition Metal Oxide crystal. This structure belongs to the R$\bar{\bar{3}}$m space group.

1.3 Thin Film Lithium Cobalt Oxide Cathodes

The typical cathode is composed of primary/secondary particle aggregates, which are kept in electrical contact by the inclusion of a carbon-based binder and conductive additives. This process is generally referred to as slurry casting. Unfortunately, these additives serve little to no benefit to the energy density of the cathode. Alternative synthesis routes, like thin film deposition techniques, have been developed to remove the presence of these additives and maximize the amount of active material in a given volume.

Lithium cobalt oxide (LCO) is an LTMO material that has received attention for thin film deposition studies.[13], [14], [15] This material is popular for its high theoretical capacity (274 mAh/g). Like other LTMOs, the structural limitations of LCO restrict its practical capacity. For LCO in particular, this value is limited to 140 mAh/g, which is about half of the total capacity. The stability of the Co^{3+}/Co^{4+} redox couple makes the thin film deposition of LCO relatively easy compared to other LTMO materials.

By controlling the rate of deposition, researchers have studied the anisotropic properties of LCO.[14], [16], [17], [18] We highlight that the following discussion on the crystallographic characterization of LCO are also consistent for other LTMO materials. As shown in Fig. 1.4, LCO has been deposited in the direction normal to three crystallographic planes: the (003), (104), and (101). We call films aligned in the direction normal to a given (hkl) plane, (hkl) textured. For (003) textured LCO, we expect lithium diffusion to primarily occur through grain boundary transport as lithium diffusion through transition metal layers is unfavorable. On the other hand, (101) and (104) textured LCO films expose lithium channels to the electrolyte, which should improve the rate capability of these films in comparison to (003) textured LCO. In fact, lithium diffusion coefficients for (104) textured LCO have been observed to be much higher than the coefficient observed for (003) textured LCO.[18] Despite the observed superior rate capability for (101)/(104) textured LCO, (003) textured LCO films have been observed to show superior capacity retention.[17] It is important to highlight that the films used for this study were approximately 350 nm in thickness; therefore, these results may not be consistent for much thicker films. Unfortunately, sputtering techniques are limited to thin film deposition as these techniques suffer from slow deposition rates.

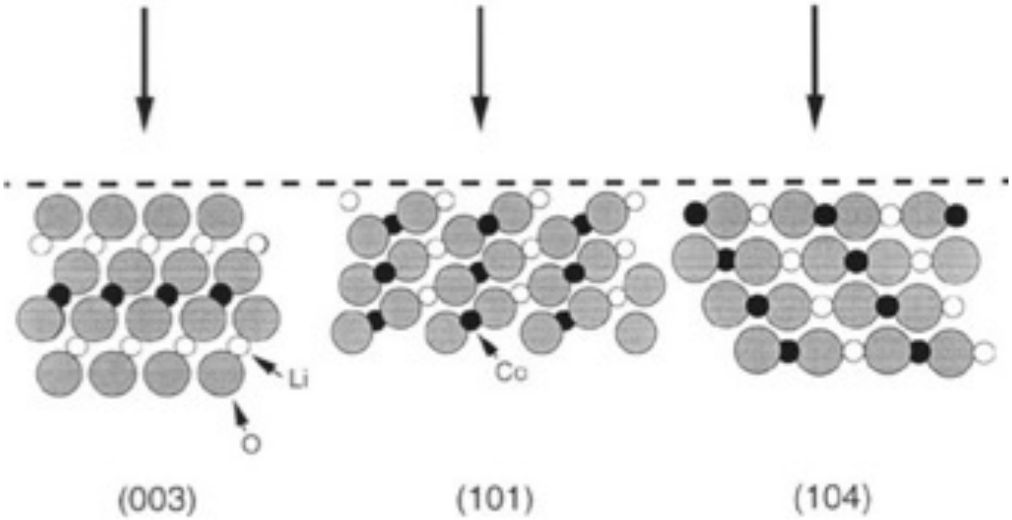

Figure 1.4: Lithium cobalt oxide is primarily deposited in the direction normal to three different crystallographic planes. This allows researchers to study the anisotropic properties of layered transition metal oxides (reproduced from [14]).

1.4 Electrodeposition of Lithium Cobalt Oxide

Electrodeposition is a promising alternative to sputtering due to its facility, scalability, and tunable control of deposit thickness and morphology. In our group, this technique has been applied to deposit almost 100% dense LCO films at thicknesses greater than 10 μm from a LiOH-KOH eutectic solution.[19] The schematic of the three electrode setup typically used for electrodeposition (Fig. 1.5) shows that electrooxidation of precursors in the solution leads to the growth of an LCO film on the working electrode. The fundamentals of this technique are discussed in further detail in **Chapter 2**, but it is important to highlight that controlling the deposition voltage will influence the morphology of the obtained deposit.

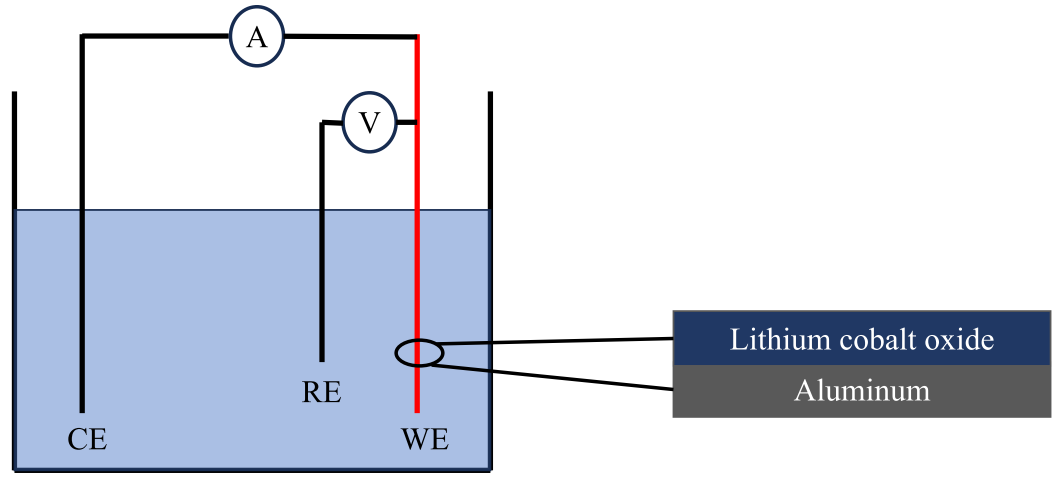

Figure 1.5: A summary of the three-electrode setup used for $LiCoO_2$ electrodeposition. The material of interest is deposited on the working electrode (WE). The reference electrode (RE) is used to measure the voltage at which the deposition takes place. The counter electrode (CE) completes the circuit. Current flow between the WE and CE is also measured or held constant during deposition.

1.5 Molten Salt Synthesis of Nickel Rich Lithium Transition Metal Oxides

As previously mentioned, the active material of the typical cathode is synthesized in the form of primary/secondary particle aggregates. Primary particles are approximately hundreds of nanometers in size and agglomerate to form secondary particles on the order of several micrometers in size. These aggregates typically include voids that impact the performance of LTMO cathode materials in several ways.[20] Firstly, the lack of continuity between grains of LTMO primary crystals leads to cathode architectures with large surface areas, which aggravate side reactions with the liquid electrolyte and lead to the relatively rapid growth of a cathode-electrolyte interphase (CEI). A thick CEI inhibits the facility of lithium diffusion between the cathode and the electrolyte. Another complication associated with primary/secondary particle aggregates of LTMO crystals is the stress accumulation and release, which occur as a result of the volume changes associated with phase change of these crystals at high voltages. The stress release leads to cracking of individual primary particles and across secondary particles.

Additionally, it is important to highlight that oxygen release occurs for this class of materials when they are charged to sufficiently high voltages.

A critical step in the development of LTMO materials was the inclusion of high degrees of nickel in the transition metal site (e.g. $LiNiO_2$, $LiNi_{0.8}Mn_{0.1}Co_{0.1}O_2$ (NMC 811)). This class of LTMO materials typically have high capacities (180-220 mAh/g) due to the multiple oxidation states available for nickel. A critical drawback for these materials is the similar ionic size of Ni^{2+} and Li^{+}, which leads to the appearance of antisite defects for these elements, often referred to as cation mixing (CM). This defect inhibits the rate capability of nickel rich LTMO materials and limits their total capacity. The issues we highlight for nickel rich cathode materials are summarized in Fig. 1.6. We note that these problems are generally applicable to other LTMO materials.

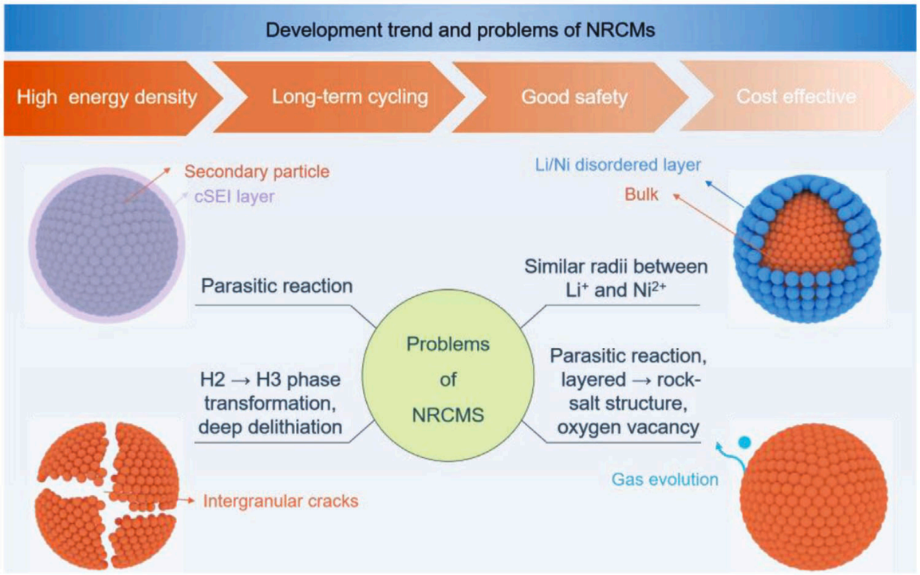

Figure 1.6: A summary of the development trend and problems associated with nickel rich cathode materials (NRCMs) (reproduced from [20]).

The difficulty associated with controlling the redox state of nickel inhibits its popularity in thin film studies. As a result, alternative routes must be explored to understand how morphology impacts the achievable capacity and cycle life of these materials. A popular method to reduce the surface area of polycrystals and to control their shape is to grow these crystals as large single crystals. The size of these crystals ranges from several hundred nanometers to several micrometers.

Numerous techniques exist to fabricate single crystals of NRCMs, but molten salt synthesis (MSS) is an attractive option due to its ease, tunability, and scalability.[21] During this process, precursors of the material of interest are added to a molten salt medium, which increases the rate at which individual crystals grow. The fundamentals of how to tune crystal shape, how to synthesize high-quality single crystalline NRCMs, and how to select precursors for the MSS process are discussed in more detail in **Chapter 3**. A general depiction of the MSS procedure is shown in Fig. 1.7.[20]

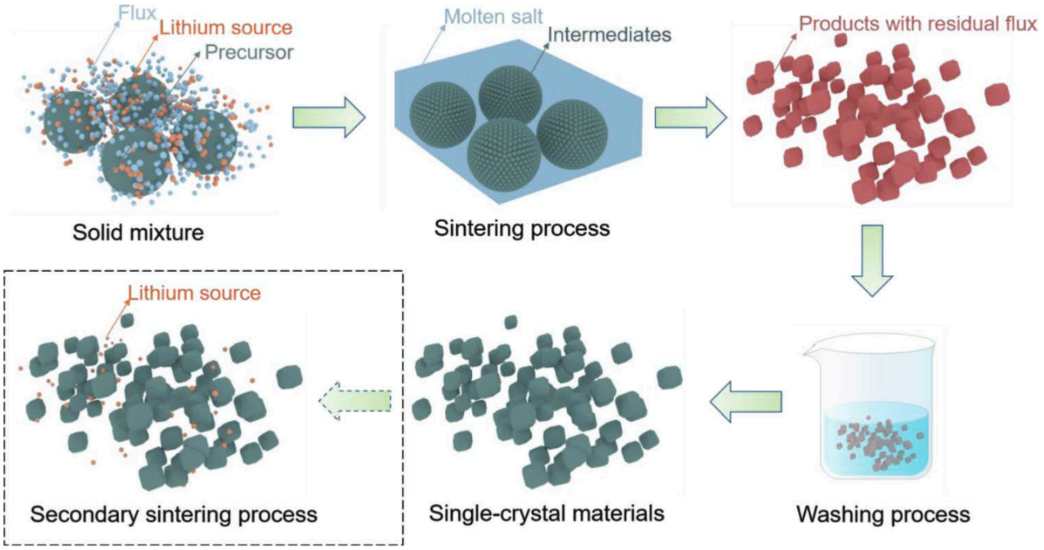

Figure 1.7: Schematic of the general procedure used for molten salt synthesis of NRCMs (reproduced from [20]).

1.6 Thesis Aim and Structure

A critical knowledge gap exists in how to best tailor the morphology of LTMO cathode materials to maximize their cycle life in LIBs. More specifically, there's a lack of data on how texture influences LTMO capacity retention when film thickness is commercially relevant. In **Chapter 2**, this thesis explores the fundamentals of electrodeposition and its application to fabricating LCO with regards to how texture can be controlled. Furthermore, how texture influences the cycle life of LTMO materials is characterized from the perspectives of interfacial and bulk changes that take place during long-term electrochemical cycling in **Chapter 4**. Due to the nascence of single crystal NRCMs research, there is also a lack of careful characterization of these materials with regards to how to best manipulate synthesis parameters to obtain a given morphology. In this thesis, we explore how to control and optimize MSS parameters in **Chapter 3**. In **Chapter 5**, we detail how the obtained morphology influences the capacity retention of the NRCM NMC 811. Lastly, in Chapter 6, we summarize the work completed in this thesis and give perspectives on future research directions in the development of single crystalline NRCMs.

CHAPTER 2: ELECTRODEPOSITION OF LITHIUM COBALT OXIDE

2.1 Introduction and Motivation

As discussed in **Chapter 1**, electrodeposition of LTMO materials is an attractive method to maximize the amount of active material in a given volume of a cathode. Over the last decade, our group has studied how electrodeposition can be applied to the fabrication of LCO films.[19] This study was the first of its kind. Since then, we have studied how deposition conditions influence the quality of the obtained deposit. The results obtained from that studied are presented in this chapter.

We detail how we discover the parameters to tune deposit quality using cyclic voltammetry. These parameters are then applied to constant voltage (chronoamptometry) depositions on aluminum substrates. Several practical synthesis considerations are offered, which include the preparation of bath materials, impact of deposition conditions on deposit morphology, and how deposit uniformity can be maintained when scaling this process up. Finally, we draw conclusions on how this process can be used to tailor cathode architectures for specific LIB applications.

2.2 Electrochemistry of the Electrodeposition Process

A potentiostat is a device used to control the voltage of the working electrode (WE).[22] This voltage is measured with respect to a reference electrode (RE). Ideally, the RE maintains a constant composition while the WE voltage changes. Electrochemical reactions occur when this voltage reaches particular values. The counter electrode is included to complete the circuit and provide an electrode for the opposing half-cell reaction to occur. An oxidation reaction occurs when an ionic species donates an electron to another species. On the other hand, reduction occurs when an ionic species accepts an electron from another species.

The suggested electrochemical reaction for the electrodeposition of LCO is shown in Eq. 2.1.[19]

$$2LiOH + 3CoO \rightarrow 2LiCoO_2 + Co + H_2O \tag{2.1}$$

In short, LCO is deposited at the WE while cobalt is deposited at the CE. The theoretical mass of deposited LCO can be calculated using Faraday's Law (Eq. 2.2)

$$m_{theo} = QA/nF \tag{2.2}$$

Here, m_{theo} is the deposited mass of LCO, Q is the net charge passed, A is the atomic weight of the deposited LCO, n is the number of electrons transferred during the deposition of one atomic unit of LCO, and F is Faraday's constant (96485 C/mol). The efficiency of the deposition process is calculated by measuring the initial substrate weight, the weight of the WE after deposition, and taking the ratio of the measured mass (m_{act}) to the theoretical mass (Eq. 2.3).

$$\eta = m_{act}/m_{theo} \tag{2.3}$$

The nucleation and growth of the electrodeposited layer is dependent on factors such as precursor concentration, reaction overpotential, and substrate material. However, we only consider the former as variables since LCO is primarily electrodeposited on aluminum substrates.

Zhang et al first completed cyclic voltammetry (CV) on the near eutectic mixture of LiOH-KOH at 260 °C. The cobalt precursor used for this deposition is cobalt oxide (CoO). This experiment and the following deposition tests are conducted under Argon gas to limit the possibility of side reactions occurring proceeding and during electrodeposition. During CV, the potential of the WE is swept in a given potential window at a constant scan rate. The user is then able to see the potential at which various reactions take place at the WE by monitoring the current flow between the WE and CE. An example scan is shown in Fig. 2.1.

As shown in Fig. 2.1, the electrodeposition of LCO occurs between 0.6-0.8 (V vs. Co). We show in Chapter 2.3 that the morphology of the electrodeposited sample is heavily influenced by the voltage that is applied during this process, among other parameters.

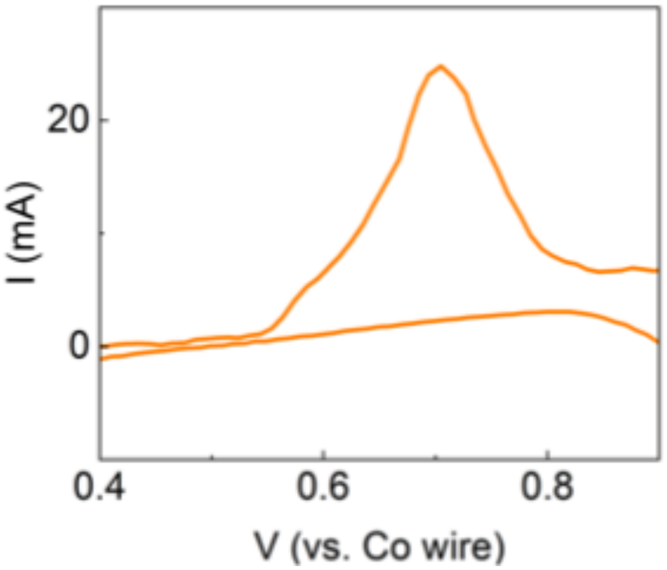

Figure 2.1: General cyclic voltammogram of $LiCoO_2$ electrodeposition. The reference electrode used for this experiment is a cobalt metal wire.

2.3 Practical Considerations for Introducing Texture to Electrodeposited Lithium Cobalt Oxide Films

A variety of factors influence the obtained morphology for electrodeposited LCO such as the substrate of choice, the precursor concentrations, and temperature during deposition. We keep these variables constant throughout the deposition process and observe the morphology obtained by varying the potential applied between 0.6-0.8 (V vs. Co). Applying a low voltage (e.g. 0.6 V vs. Co) favors film deposition in the direction normal to the (003) plane while applying a higher voltage (e.g. 0.8 V vs. Co) favors the deposition of films in the direction normal to the (104) plane. The former deposits are referred to as (003) LCO while the latter deposits are referred to as (104) LCO deposits.

(003) LCO deposits consist of platelets aligned normal to the microscope, while (104) LCO deposits consist of platelets aligned vertically to the microscope.

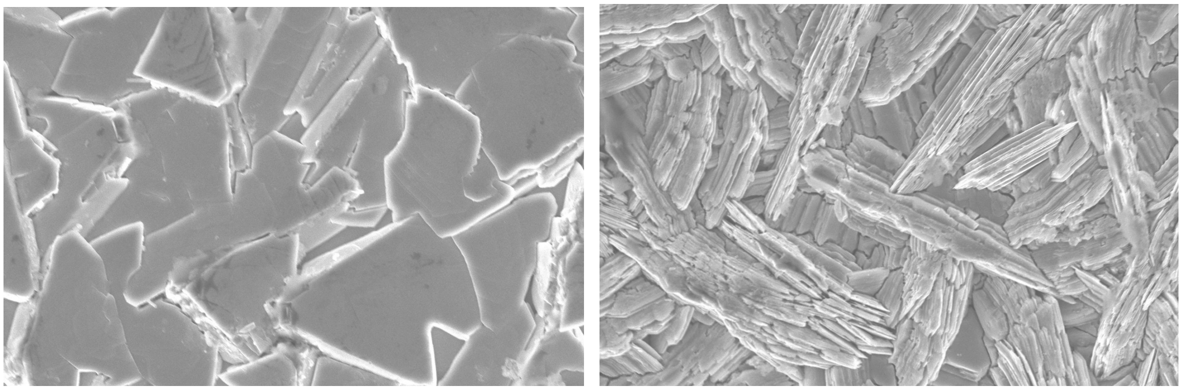

Figure 2.2: Scanning electron microscopy images of LCO applied at 0.6 V (vs. Co) (left) and at 0.8 V (vs. Co) (right).

Following the electrodeposition process, the obtained deposits are washed using deionized water under constant agitation. To eliminate any potential damage to the deposit surface, these obtained deposits are then annealed at 550 °C for 5 hours in air. We then confirm the texture of the obtained deposit using X-ray diffraction (XRD). Examples of diffraction patterns for (003) and (104) LCO are shown in Fig. 2.3. It is apparent that the observed (003) peak for (003) LCO is the main contributor to the observed intensity while the (104) is the most intense peak observed for (104) LCO.

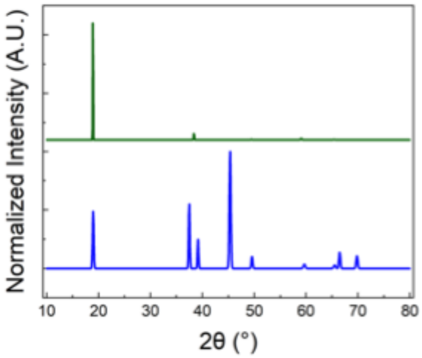

Figure 2.3: X-ray diffraction patterns of LCO. LCO obtained using 0.6 V (vs. Co) (green) and 0.8 V (vs. Co) (blue).

2.4 Conclusions

In this chapter, we introduced the fundamental concepts that influence the electrodeposition of LCO. We discuss the conditions at which a given deposit is obtained, as well as how electrodeposited films are characterized. Our voltametric studies confirm LCO can be deposited on aluminum substrates and that the texture of the deposit can be altered by controlling the deposition voltage. Based on this work, the influence of the film texture on the long-term stability of LCO deposits can be observed (mention further studies on deposition in future work). This influence is the subject of interest for **Chapter 4**.

CHAPTER 3: MOLTEN SALT SYNTHESIS OF SINGLE CRYSTALLINE NICKEL RICH LITHIUM NICKEL MANGENESE COBALT OXIDES

3.1 Introduction and Motivation

We highlighted in **Chapter 1** the conventional morphology of a composite cathode. We also detailed the drawbacks of primary/secondary aggregates for the long-term cycle life of an LIB cathode. A nascent research direction is the growth of single crystalline NRCMs like NMC 811 ($LiNi_{0.8}Mn_{0.1}Co_{0.1}O_2$).[20], [23], [24], [25] The lack of detailed procedures and studies on NRCMs makes studying the improvement of single crystal synthesis critical to the future of cathode materials.

A relevant tool for evaluating the quality of single crystalline NRCMs is the degree of cation mixing (CM) present in the as made crystal.[26] This is critical as single crystals with a high degree of CM suffer from lower initial capacity and more rapid capacity fade than single crystals with reduced mixing.

Here, we detail how we developed our own procedure to synthesize high quality NMC 811 using molten salt synthesis (MSS). We use variables such as precursor concentration, synthesis temperature, and choice of flux as parameters to control the synthesis of this material. We show that using XRD to observe the degree of CM present is critical in evaluating the quality of synthesized NMC.

3.2 Chemistry of the Molten Salt Synthesis Process

MSS is an alternative to solid state synthesis for cathode materials. This method is primarily beneficial because of increased reaction kinetics in the liquid medium compared to what is observed for solid state reactions. Moreover, the use of a liquid medium can also lower the synthesis temperature.

Kimijima et al suggested a reaction pathway for the MSS of $LiNi_{0.33}Mn_{0.33}Co_{0.33}O_2$ (NMC 111).[24] Here, we apply their equation to describe the synthesis of NMC 811 (Eq. 3.1).

$$Ni_{0.8}Mn_{0.1}Co_{0.1}(OH)_2 + LiOH \cdot H_2O + flux + \frac{1}{4}O_2 \rightarrow LiNi_{0.8}Mn_{0.1}Co_{0.1}O_2 + flux + \frac{5}{2}H_2O \quad (3.1)$$

As shown in eq. 3.1, the stoichiometric hydroxide $Ni_{0.8}Mn_{0.1}Co_{0.1}(OH)_2$ can be used to directly synthesize NMC 811. We note that this precursor can be formed in situ through the breakdown of stoichiometric amounts of precursors like nickel nitrate. The flux used for this synthesis process includes salts such as nitrates, sulfates, and acetates.

MSS can be described in a series of steps. Proceeding the liquification of the flux, this system exists in the solid state. After the flux liquifies, Kimijima et al hypothesize that nuclei of NMC 811 form around 500 °C. When the synthesis temperature is held above this value, single crystal growth proceeds via the Ostwald ripening process, where smaller nuclei redissolve into the molten salt medium and crystallize onto larger crystals. Moreover, they indicate that the lithium precursor for this process can be lithium hydroxide or lithium oxide.

Although this process can be described quite simply, careful consideration of the synthesis environment must be taken to limit cation mixing. An important limitation of the MSS of NRCMs is that the synthesis typically must take place under an oxygen rich atmosphere. This is a problem because it increases the cost associated with preparing high quality cathode materials. How we took inspiration from Mesneir et al to alleviate this issue is the subject of the next section of this chapter.[27]

3.3 Heuristics of the Molten Salt Synthesis of NMC 811 Single Crystals

A heuristic technique is an approach to problem solving that involves a pragmatic approach to a nonoptimized issue. In the case of MSS, this approach was applied by Mesneir et al to discover how they could minimize CM in the LTMO lithium nickel oxide. Their experimental procedure involved tuning their lithium precursor, synthesis temperature, and synthesis time. Herein, we apply a similar approach to optimize the synthesis of NMC 811 in air. We first describe why CM occurs from a solid-state perspective.

3.3.1 Solid State Ionics of Cation Mixing in NRCMs and Alleviating Mixing in the Liquid State

Solid state ionics are concerned with the motion of mobile ions in the solid state. Obviously, many solid-state reactions can become more facile at high temperatures. Typically, Kröger–Vink notation is used to categorize a given reaction. When an ion is in the correct site, one simply uses the element name, a subscript of the element, and the superscript “x” (e.g. Nickel at a Nickel site is Ni^{x}_{Ni}). This notation indicates that there is no charge that deviates from the normal state for this site. A vacancy, that is, when no ion is present where one should be, is denoted using a “V”. An antisite defect occurs when a different ion is found at a site than one would expect (e.g. when Li^{+} occupies an Ni^{2+} site). When antisite defects occur, the charge associated with a particular site can deviate from its expected value. For example, when Ni^{2+} is present at an Li^{+} site, the positive charge associated with this defect is denoted using a “•”. This situation is overall indicated using $Ni^{\bullet}_{Li}$. If instead Ni^{3+} was present at an Li^{+} site, this defect would be denoted as $Ni^{\bullet\bullet}_{Li}$. On the other hand, when Li^{+} is present at an Ni^{2+} site, the negative charge associated with this defect is illustrated using a “′”. This notation is critical to define so that we can develop a holistic understanding of CM in NRCMs.

Orlova et al described the solid state reactions that dictate CM in NRCMs.[28] This antsite defect is favorable at high temperatures due to the similar ionic radii of Ni^{2+}(0.69 Å) and Li^{+}(0.76 Å). This defect is described in Eq. 3.2.

$$Ni^{x}_{Ni} + Li^{x}_{Li} \rightarrow Li'_{Ni} + Ni^{\bullet}_{Li} \tag{3.2}$$

A method for reversing this issue is to anneal or synthesize NRCMs in an oxygen rich environment. The solid-state reaction that drives this solution is shown in Eq. 3.3.

$$Ni_{Ni}^{x} + 2Li(s) + O_2(g) \rightarrow Li_{Ni}' + Ni_{Ni}^{\bullet} + Li_{Li}^{x} + 2O_O^{x} \tag{3.3}$$

As shown in Eq 3.3, Ni^{2+} can be oxidized to Ni^{3+} in the presence of oxygen, thus eliminating the contamination of lithium sites in these materials. This elimination is imperative to preserving the long-term cyclability of NRCMs. However, MSS occurs via a liquid medium and molten salts tend to block the diffusion of gaseous oxygen into this medium. As a result, it is imperative that precursors that release oxygen upon their decomposition are chosen for flux components.

It is important to highlight the decomposition reaction of the lithium precursors of interest for this study. These salts include lithium hydroxide (Eq. 3.4), lithium oxide (Eq. 3.5), and lithium nitrate (Eq. 3.6).

$$2LiOH(s) \rightarrow Li_2O(s) + H_2O \tag{3.4}$$

$$4LiNO_3(s) \rightarrow 2Li_2O(s) + O_2(g) + 4NO_2(g) \tag{3.5}$$

$$2Li_2O_2(s) \rightarrow 2Li_2O(s) + O_2(g) \tag{3.6}$$

These decomposition reactions each onset at different temperatures. For LiOH, the decomposition temperature is around 900 °C. The lack of oxygen release for this salt during decomposition justifies Qian et al's assertion that LiOH is not an highly oxidative salt.[29]

3.3.2 Synthesizing and Characterizing NMC 811

In this section, the experimental procedure for synthesizing NMC 811 is detailed. We first cover how XRD can be used to characterize the extent of CM in synthesized NMC 811 single crystals. Following this, the route to synthesize high-quality NMC 811 single crystals using different molten salts and lithium precursors is explained.

XRD is an effective technique to confirm the crystallinity of an obtained NMC powder. The ICSD diffraction pattern for NMC 811 is shown in Fig. 3.1. In this figure, it is clear that several diffraction peaks appear in the obtained pattern. However, the most relevant peaks for NMC 811 are the (003) and the (104) peaks.

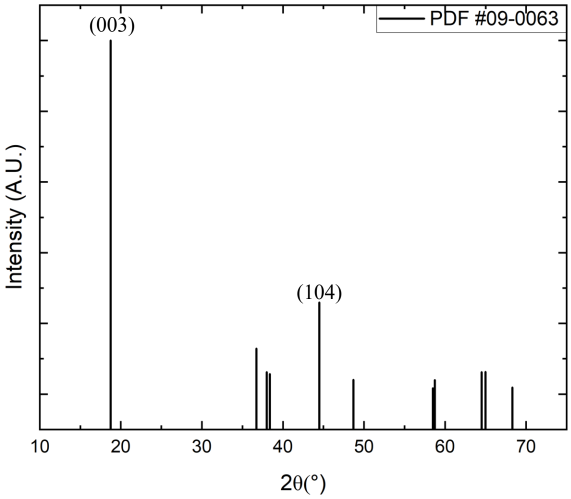

Figure 3.1: Standard XRD pattern for NMC 811.

As previously stated, using XRD, the extent of CM present in NRCMs can be calculated. These calculations were obtained for NMC 811 by Telchert et al by taking the peak intensity ratio of the (003) and (104) diffraction peaks for a given powder.[30] They calculated the percentage of CM when the ratio is between 1.5 and 1. As illustrated in Fig. 3.2, the percentage of CM approaches 0% as the (003)/(104) intensity ratio approaches 1.5. Conversely, as this ratio approaches 1, the percentage of CM approaches 10%. This tool is invaluable for screening powders for their quality.

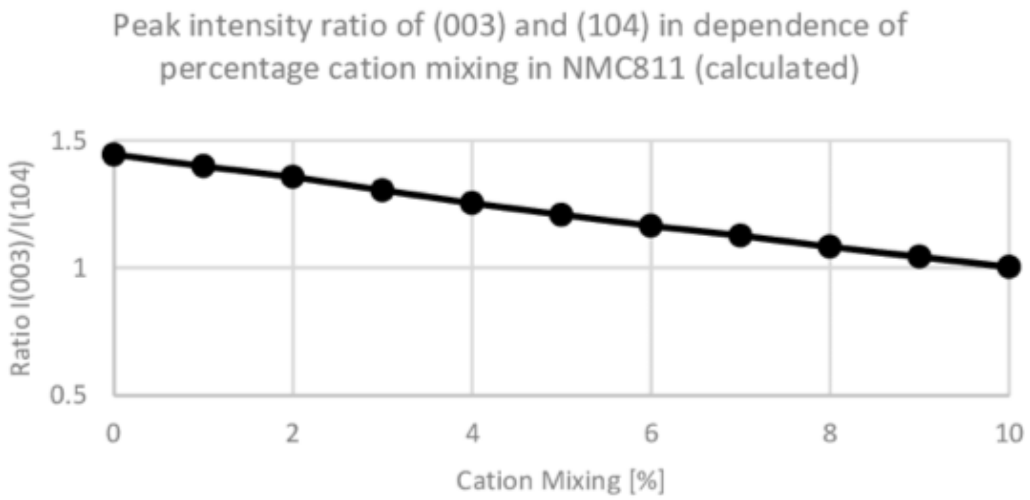

Figure 3.2: Cation mixing as a function of the (003)/(104) intensity ratio for NMC 811 (reproduced from [30]).

In the following section, this graph is used as a tool to evaluate the quality of our crystals. This tool is first applied to NMC 811 synthesized using chloride fluxes. Afterwards, we detail our process for finalizing the flux of choice for air synthesis of NMC 811.

Chlorides are a popular option as a flux for MSS since the melting points of the pure substances and their eutectics are comparatively lower than other options, such as sulfates. Other options for fluxes, such as nitrates, also have low melting points but degrade at lower temperatures as well. The first fluxes of choice for MSS of NMC 811 in this study were cesium chloride and potassium chloride. We were interested in observing how these two fluxes would influence the obtained single crystal morphology. The lithium precursor used for these samples was lithium nitrate. Moreover, the transition metal precursor was $Ni_{0.8}Mn_{0.1}Co_{0.1}(OH)_2$. An optical image of the precursor mixture is shown in Fig. 3.3. Details of the synthesis procedure are included in the Experimental Methods section of this chapter.

Figure 3.3: Precursor mixture of NMC 811.

Following a washing procedure, we collected SEM images of the as-synthesized powder. These images are shown for NMC 811 synthesized in CsCl and KCl, respectively.

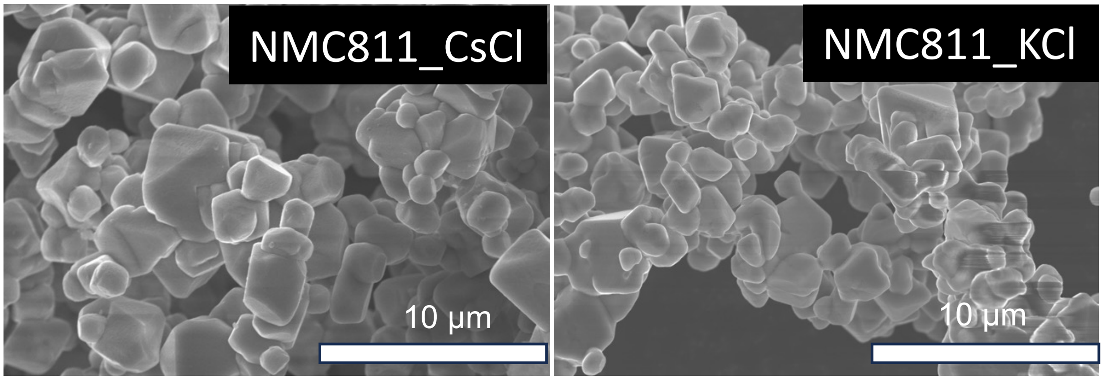

Figure 3.4: SEM images of NMC 811 synthesized in CsCl (left) and KCl (right).

It is apparent that the geometry of NMC 811_CsCl single crystals is the truncated octahedron while there is no preferred geometry for the NMC_KCl single crystals. A deeper look at the geometry of the synthesized single crystals is taken in the next section of this chapter. The measured diffraction patterns for these crystals is shown in Fig. 3.5.

Examining Fig. 3.5, it is apparent that each of these samples contains a degree of mixing that is greater than 10% as the (003)/(104) intensity ratio, labeled "j", is less than 1 for both samples. Several iterations were made on the synthesis temperature, but this proved inconsequential to the observed j. As a result, we looked to a heuristics paper on $LiNiO_2$ for inspiration.[27] Using, their combination of LiOH, $LiNO_3$, and Li_2O_2, NMC 811 with an improved ratio was synthesized (Fig. 3.6).

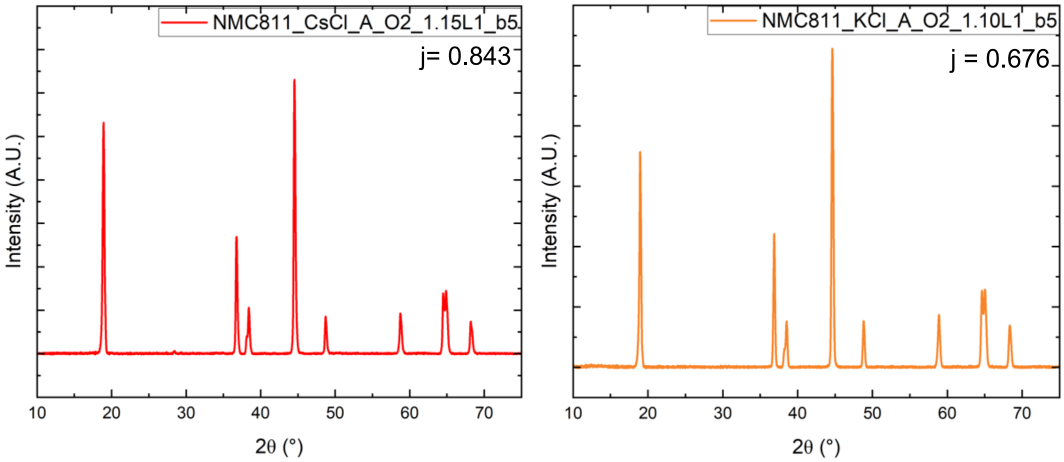

Figure 3.5: XRD patterns of NMC 811 synthesized in CsCl (left) and KCl (right). The intensity ratio of the (003) and (104) peaks is included as the parameter j.

Examining Fig. 3.6, it is apparent that j is improved for samples synthesized with more oxidative salts, but the ratio remains less than 1. This conclusion led us to consider using a different flux entirely. Moiseev et al. found success using lithium sulfate as a flux, so this salt was used as a flux for MSS.[31] A flux iteration with a lithium sulfate potassium sulfate eutectic was also used to see if the lower melting point of the flux would improve the quality of the synthesized single crystal. The obtained XRD patterns for this iteration of NMC 811 are shown in Fig. 3.7. We highlight that the lithium salt for these samples was lithium hydroxide.

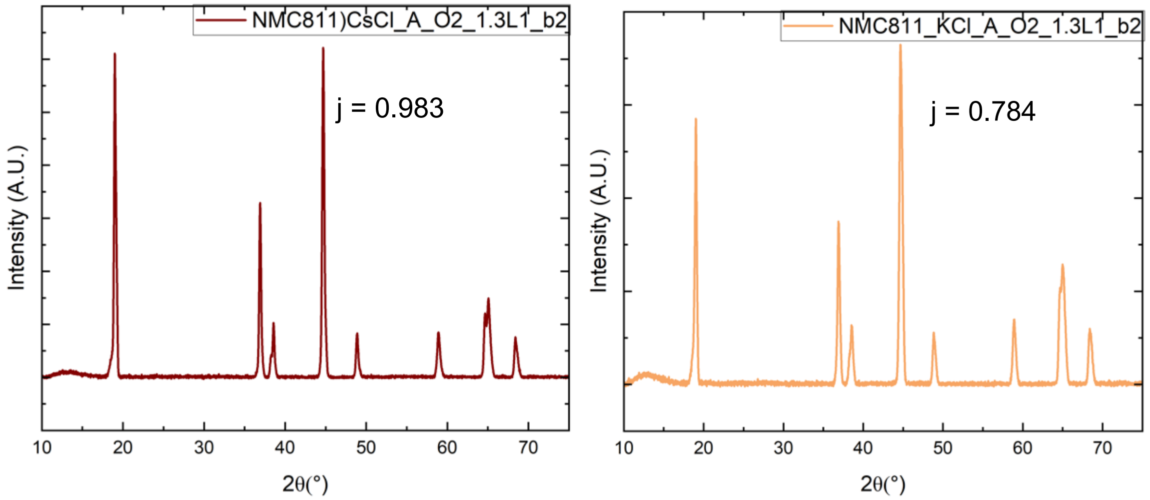

Figure 3.6: XRD patterns of NMC 811 synthesized in CsCl (left) and KCl (right). The intensity ratio of the (003) and (104) peaks is included as the parameter j.

Analyzing Fig. 3.7, it is apparent that the degree of CM is improved in these samples in comparison to our NMC 811 synthesized in the chloride fluxes. Since we observed an improved j ratio for the optimized lithium salt, we iterated our salts. We found that the best samples were made using a combination of lithium hydroxide and lithium nitrate (Fig. 3.8).

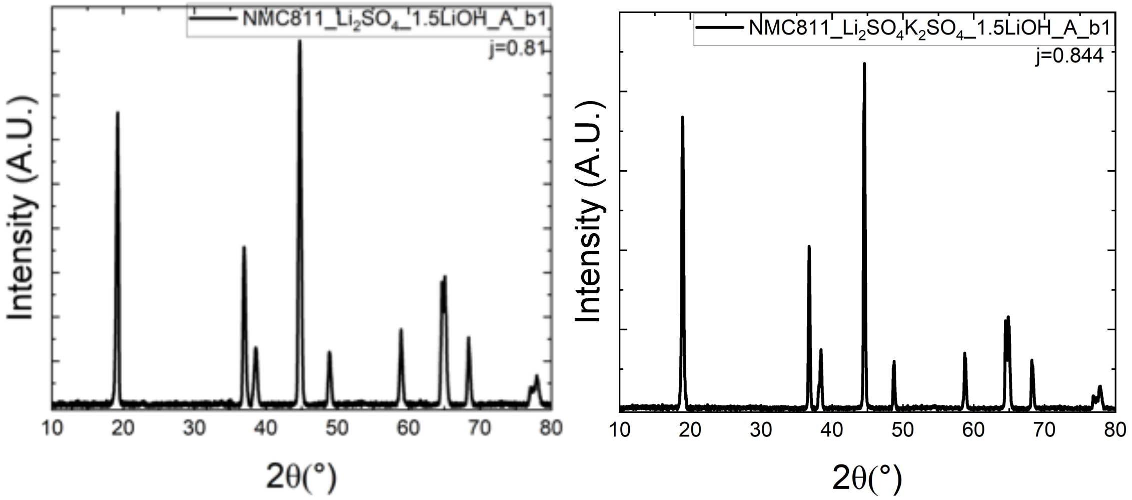

Figure 3.7: XRD patterns of NMC 811 synthesized in Li_2SO_4 (left) and Li_2SO_4-K_2SO_4 (right). The intensity ratio of the (003) and (104) peaks is included as the parameter j.

From Fig. 3.8, we observe that the combination of a sulfate flux and lithium precursor with sufficient oxidative power facilitates the synthesis of NMC 811 with a low degree of CM. Further improvements for reducing CM in NRCMs are suggested in **Chapter 6**.

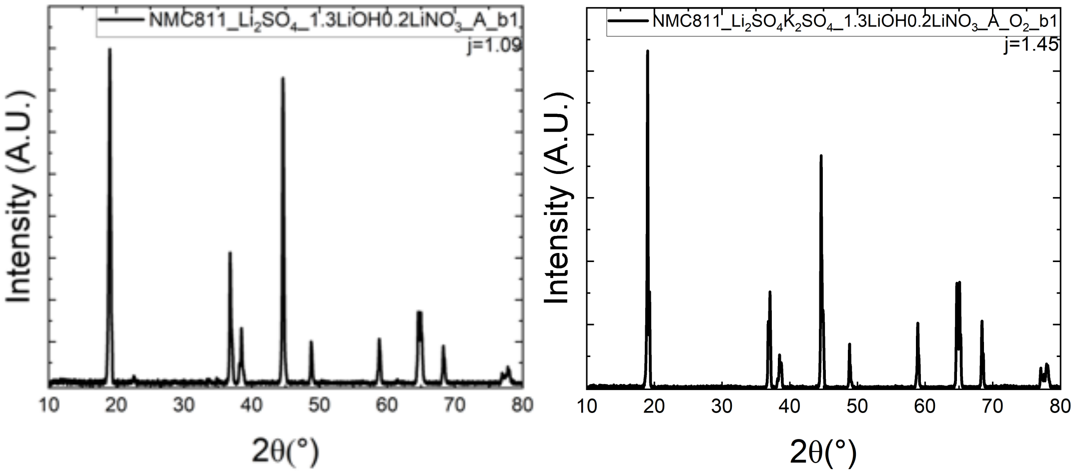

Figure 3.8: XRD patterns of NMC 811 synthesized in Li_2SO_4 (left) and Li_2SO_4-K_2SO_4 (right). The intensity ratio of the (003) and (104) peaks is included as the parameter j.

3.4 Practical Considerations for Controlling the Morphology of Nickel Rich Lithium Transition Metal Oxide Single Crystals

So far, the heuristic approach to synthesizing high-quality NMC 811 in air via MSS has been outlined. This is important to note since this synthesis must typically be completed in a pure oxygen environment. Here, it is detailed how the morphology of NMC 811 single crystals can be manipulated to expose particular facets. This is imperative to tailoring the synthesized crystals for specific applications. First, the typical facets observed for NRCMs are illustrated. The benefits of using a particular facet of NMC are also described.

The crystal facets typically observed for NRCMs include the (001), (012), and (104) facets. The ionic species present at the terminated surfaces of these facets and their surface energies are illustrated in Fig. 3.9.[32]

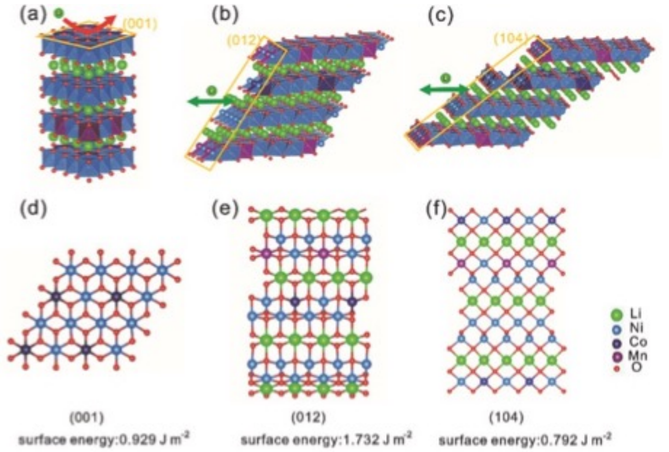

Figure 3.9: Equilibrium facets for NRCMs. (a): NMC 811 single crystal aligned in the direction normal to the (001) plane. (b): Li^+ diffusion in the direction normal to the (012) plane of an NMC 811 single crystal. (c): Li^+ diffusion in the direction normal to the (104) plane of an NMC 811 single crystal. (d)-(g): Surfaces and surface energies for the (001), (012), and (104) facets for NMC 811, respectively. (reproduced from [32]).

Analyzing Fig. 3.9, it is apparent that lithium-ions diffuse in the direction parallel to the (001) plane for NRCMs. Moreover, it is also apparent that the (012) and (104) facets allow lithium diffusion in the out of plane direction. As seen in Fig. 3.9e, the (012) facet has the highest observed surface energy of the three predominant NRCM facets. Furthermore, as shown in Fig. 3.9f, the (104) facet has the lowest surface energy. The high surface energy and tendency for lithium to diffuse through the (012) surface influences the growth of a thick CEI on these surfaces. NRCMs terminated with predominantly (104) facets have low surface energies, CEIs still form on these surfaces due to these facets being facile for lithium diffusion, although to a lesser extent than NRCMs with dominant (012) surfaces.[33]

The single crystal geometries typically observed for NRCMs are shown in Fig. 3.10.[26] As seen in this figure, the obtained single crystal is a function of the synthesis environment. Highly oxidizing environments favor the growth of single crystals with a predominately (012) surface area, while synthesis environments with a low lithium activity favor the growth of single crystals with a surface predominately terminated by the (001) plane. Moreover, synthesis environments with a low oxygen activity favor the growth of single crystals with predominately (104) surface areas. However, it is also important to highlight that the obtained single crystal is also dependent on the flux used, as seen in the previous section of this chapter with CsCl and KCl. From Fig. 3.10, it is revealed that the NMC 811 single crystals obtained using a CsCl flux are predominately truncated octahedrons. For KCl, we look to the results obtained by Kim et al.[34] They conclude that NMC 811 synthesized using a KCl flux are typically in an isotropic form. That is, these single crystals exhibit no preferred geometry.

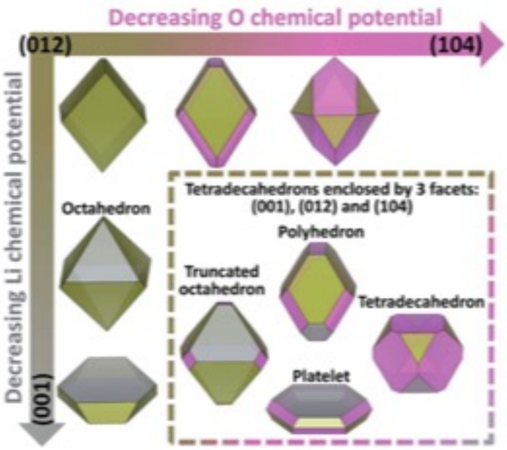

Figure 3.10: The dependence of observed single crystal on the synthesis environment (reproduced from [26]).

In Fig. 3.11, we show the single crystals obtained using our optimized sulfate fluxes. Here we include the addition of a dopant, molybdenum, to observe the impact of its inclusion on the resulting single crystal morphology.

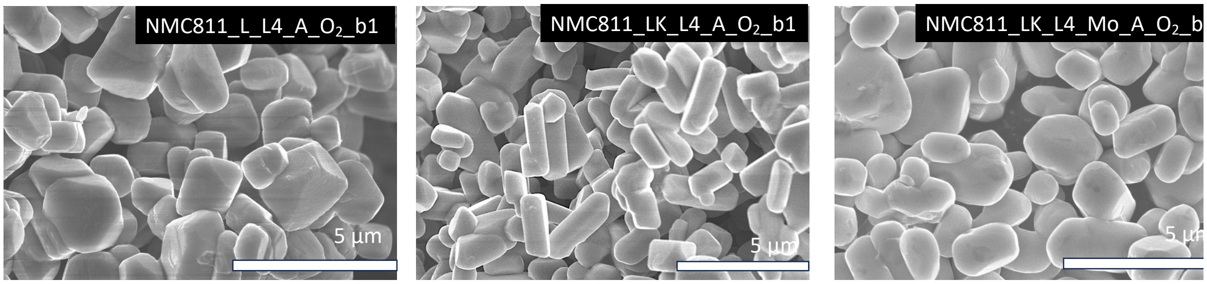

Figure 3.11: The dependence of observed single crystal on the synthesis environment for a Li_2SO_4 flux (left), Li_2SO_4-K_2SO_4 flux (middle), and Li_2SO_4-K_2SO_4 flux with MoO_3 addition (right).

From Fig. 3.11, it is apparent that the composition of the bath is influential in determining the morphology of the obtained single crystals. Viewing Fig. 3.11a, it is apparent that the single crystals synthesized using lithium sulfate belong to the truncated octahedron class. The crystals obtained using a Li_2SO_4-K_2SO_4 eutectic are isotropic in shape, similar to what Kim et al. observed for the KCl flux. Moreover, the addition of MoO_3 changes the equilibrium shape of the NMC 811 single crystals to highly dispersed crystals, which are similar to those observed by Huang et al.[35] They assert that these crystals are predominately terminated by (104) facets.

3.5 Conclusions

The goal of this chapter was to outline the motivations and rationale for developing MSS of NRCMs. We specifically detail how to use this technique to synthesize NMC 811. Moreover, the parameter space for reducing CM in this cathode material and the implications of the precursor solution on the morphology of the resulting single crystals are discussed. These materials are implemented in half-cells to reveal whether the single crystal morphology impacts the stability of an LIB cathode in Chapter 5.

3.6 Experimental Methods

NMC 811 Molten Salt Synthesis: The flux used for molten salt was either Li_2SO_4 or K_2SO_4-Li_2SO_4 (20 mol % K_2SO_4, 80 mol % Li_2SO_4). The flux was 9.1 mol % of the total mols used during the synthesis procedure. The transition metal precursor used was $Ni_{0.8}Mn_{0.1}Co_{0.1}(OH)_2$ (NMC 811-OH). For lithium, LiOH-$LiNO_3$ was the precursor (130 mol % LiOH, 20 mol % $LiNO_3$, these percentages are relative to the transition metal precursor concentration). An optimized ramping procedure was used to fabricate each batch of single crystals. Briefly, in a tube furnace, the precursor mixture, which was contained in an alumina crucible, was elevated from room temperature to 200 °C and held the mixture at this temperature for 2 hours. Afterwards, the temperature was raised to 900 °C in 3 hours and held the mixture at this temperature for 1 hour. This mixture was then allowed to cool to 775 °C in 2 hours, where it was held at this temperature for 13 hours. Following this hold, the mixture was cooled to 300 °C in 3 hours. After this step, the mixture was allowed to cool to room temperature naturally. The synthesized powder was obtained by washing the final mixture in deionized water. This powder was then centrifuged to separate it from the water. Finally, this powder was annealed at 750 °C for 3 hours under flowing oxygen to alleviate any surface degradation induced by the washing procedure.

X-Ray Diffraction (XRD) Studies: XRD data were collected using a Bruker D8 Advance at 45 kV and 40 mA current. The XRD data were collected every 0.01 2θ using a scan speed of 0.01 °/sec. The laser wavelength was $CuK_{œ}$=1.5406 Å. The total relative contribution of the (003) reflection to the total measured intensity.

CHAPTER 4: CYCLE LIFE STUDIES OF ELECTRODEPOSITED LITHIUM COBALT OXIDE

4.1 Introduction and Motivation

As detailed in **Chapter 1**, a major focus of energy storage research has been to increase the cathode cycle life given the direct impact of cycle life on many use cases for secondary batteries. Numerous reports have determined that the development of state of charge heterogeneity with increasing cycle numbers in LTMO cathodes is a major factor that limits the cycle life of LIBs.[36], [37], [38] To form a typical cathode, LTMO particles are combined with polymeric binders and conductive additives and slurry-cast as a 10s of micrometers thick layer on a metallic (typically aluminum) current collector. Studies on slurry-cast LTMO films revealed that the formation of intergranular cracks in secondary particles during electrochemical cycling and structural degradation are connected to state of charge heterogeneity observed in these cathodes as cathode films become lithium deficient,[39] however, because the particles are randomly oriented (or nearly so) on the current collector, and generally polycrystalline, the impact of crystallography is difficult to determine.

A cathode fabrication approach we have focused on is electrodeposition.[19] LTMO cathodes formed via electrodeposition can be nearly 100% dense, highly textured, and are binder and conductive additive free. Elimination of most of the pores, as well as the binder and conductive additives in cathodes offers the potential of an increased energy density. From a fundamental perspective, since there is no binder or conductive additive, it is easier to perform studies such as Raman imaging to investigate charge heterogeneity during cycling. Because electrodeposition provides control over crystallographic orientation (texture) of the LTMO,[16], [40] studies on the effect of crystallographic texture and surface crystallography, such as reported here, are possible. In addition, relatively little is known about the development of state of charge heterogeneity during cycling of electrodeposited LTMO and its dependence on texture.[41], [42], [43] Studies to date on the effect of electrode texture on the cycling performance and charge heterogeneity in cathode materials are limited to sub-micron thick films grown via vapor-phase processes with low areal loadings[44] and extrapolation of data from such thin films to films of commercially relevant thickness is difficult if not impossible.

Of specific interest to us is the important LTMO $LiCoO_2$ (LCO). Prior to our studies, investigations on textured LCO has focused on thin films fabricated via sputtering and laser deposition techniques.[16], [40] Using films around 350 nm in thickness, Xia et al. found that (104) oriented LCO thin films ((104) LCO) exhibit Li-diffusion an order of magnitude faster than LCO thin films grown in the (003) direction ((003) LCO).[16] This difference is due to the alignment of fast Li diffusing channels normal to the substrate in (104) LCO. Li diffusion normal to [003] planes in LCO is sluggish as Li transport in the (003) oriented deposits occur primarily through grain boundaries since Li diffusion through the CoO_6 layers is thermodynamically unfavorable.[40] Despite the sluggish Li diffusion kinetics in the c-axis oriented films, (003) LCO thin films have shown superior capacity retention in comparison to (101) LCO thin films, which are also expected to exhibit facile kinetics[17] which is attributed to the increased stability of films with a relatively smaller electroactive surface area. Here we seek to understand how and why charge heterogeneity develops in thick dense electrodeposited cathodes and the influence of charge heterogeneity on the cycle life of LCO electrodes. This information will provide insight into the practical limitations of thick, e.g., >10 μm (> 1 mAh/cm^2) textured LTMO electrodes as well as fundamental information on the impact of texture on charge heterogeneity and capacity fade.

As x decreases from 1 to 0.5, the c-axis lattice parameter of Li_xCoO_2 increases by about 3% while the a-axis lattice parameter decreases by 0.35%.[45] As LCO reaches 100% state of charge ($Li_{0.5}CoO_2$), the unit cell transitions from hexagonal to monoclinic crystal structure. These anisotropic lattice changes cause an overall 1.8% increase of the unit cell volume.[46] We note, given their brittle nature, changes in volume greater than 0.1% are considered severe for LTMO materials.[39], [47] As the LCO unit cell volume increases, there is a concurrent accumulation of tensile stress in the c-axis and compressive stress in the ab plane.[48] This stress has negligible impact on the capacity of LCO in the first several cycles; however, using XRD, the c lattice parameter of LCO has been shown to permanently increase after as few as ten cycles[49] The mechanical properties of LCO also depend on the state of charge of this material. The ultimate strength (the maximum stress before fracture) of Li_xCoO_2 in the ab plane is higher than normal to the ab plane (parallel to the c-axis) in the range of $0.5 < x < 1$. Upon delithiation, the ultimate strength of LCO decreases in both directions, reaching a minimum at $Li_{0.5}CoO_2$ (4.2 V vs. Li/Li^+). The c-axis is the preferential plane for crack formation in LTMO as the deformation along the c-axis and the decrease in the ultimate strength measured along the c-axis are more significant than what is measured along the ab plane.[50],[51] Despite these findings, the interplay between charge heterogeneity, mechanical integrity, and crystallographic orientation remains unclear when film thickness is increased to achieve commercially viable loadings. It seems plausible that aligning LTMO films to expose lithium diffusion planes to the electrolyte will decrease the accumulation of stress, charge heterogeneity, and fade in cathode materials during electrochemical cycling, but there is currently a dearth of data to support this assertion. Our goal is to elucidate factors that lead to degradation of LTMOs during electrochemical cycling. A common way to investigate state of charge heterogeneity propagation in LTMOs with sub-micron spatial resolution is confocal Raman spectroscopy. The sensitivity of Raman spectra to the state of charge in many LTMOs makes confocal Raman spectroscopy a powerful technique for detecting of inactive LTMO phases in postmortem electrodes.[52][53] The most prominent Raman modes that appear in pristine LTMO materials are the E_g and A_{1g} modes.[54], [55] The E_g mode arises from metal-oxygen (M-O) vibration in the ab plane, while the A_{1g} mode arises from M-O vibration in the c-axis of LTMO materials. In particular, the Raman spectra of pristine LCO (3.0 V vs. Li/Li$^+$) exhibit strong A_{1g} and E_g modes at 590 cm^{-1} and 480 cm^{-1}, respectively. The E_g and A_{1g} modes of Li_xCO_2 attenuate during charging of this material (as x decreases).[52] These modes reappear during discharge, unless the imaged region has become electrochemically inactive, for example due to becoming electrically disconnected from the electrode as a result of grain cracking. In situ Raman spectroscopy show that a strong A_{1g} vibrational mode at 670 cm^{-1} appears in the LCO spectra at 4.2 V (vs. Li/Li$^+$).[52], [56], [57] Matsuda et al. assigned this peak to Co_3O_4 that forms during the degradation of de-lithiated (charged) LCO due to laser exposure. We note that the information of local LCO chemistry we acquire using Raman spectroscopy cannot be obtained using alternative imaging techniques, such as scanning transmission electron microscopy, which requires a very thin sample, or scanning electron microscopy (SEM), which does not provide accurate information on the state-of-charge due to the low atomic number of lithium. In this Chapter, confocal Raman spectroscopy is used to evaluate the development of charge heterogeneity after cycling in highly textured LCO electrodes, filtering for the 590 cm^{-1} and 670 cm^{-1} Raman modes to differentiate between discharged and charged regions present in postmortem cathodes. We additionally use electrochemical impedance spectroscopy (EIS) to understand the changes that arise in interfacial processes of cathode materials during cycling. The novelty of using dense cathodes for long-term studies is revealed by comparing our results to a cathode which includes the traditional binders and conductive additives.

Using EIS, the process of charge transfer in LTMO cathodes can be modeled with equivalent circuits. The charge transfer process of LCO de-lithiation consists of three steps.[58]

$$LiCoO_2 \rightarrow xLi^+ + xe^- + Li_{1-x}CoO_2 \qquad \text{(Eq. 4.1)}$$

$$Li^+ \xrightarrow{CEI} Li^+ \qquad \text{(Eq. 4.2)}$$

$$Li^+ \rightarrow Li^+ \cdot (solv.)_n \qquad \text{(Eq. 4.3)}$$

During discharge, Li^+ and e^- exit the LCO lattice, as detailed in Eq. 4.1. In Eq. 4.2 it is shown that the de-intercalated Li^+ then transports through the cathode-electrolyte interphase (CEI), which is primarily formed as the electrolyte decomposes on the cathode surface in the first few cycles. Finally, in Eq. 4.3, the Li^+ that has traveled through the CEI is solvated as it passes into the electrolyte. This solvated lithium is then transported to the anode where it undergoes another charge transfer reaction to neutralize electrons that travel through the external circuit. We apply the circuit model previously used by Dai et al to reveal how film texture influences the charge transfer process of electrodeposited LCO. The measured spectra consists of two semicircles in the mid frequency region (0.1 Hz < f < 1000 Hz) and Warburg element in the low frequency region. The width of the lower frequency semicircle is assigned to the cathode resistance to charge transfer (R_{CT}). R_{CT} is an indication on the ease of Li-ion exchange at the interface between the active material surface and the electrolyte. This parameter represents the facility of step 1. R_{CT} growth occurs due to the loss of the active area of the charge transfer interface,[59] which most readily occurs at high voltages due to the fragility of LTMOs in this state.[37], [59], [60] The width of the higher frequency semicircle is attributed to the resistance of the cathode-electrolyte interphase (R_{CEI}). R_{CEI} reflects the resistance to lithium transport through the CEI.

R_{CEI} growth occurs if the CEI thickness increases during electrochemical cycling. We expect the measured R_{CEI} value of (104) LCO to be stable during long-term cycling due to the low surface energy of this facet. Finally, the process shown in step 3 is typically modeled as the Warburg impedance. The Warburg impedance indicates the facility of Li^+ transport in the bulk cathode.[60] A cathode exhibiting mass transport limitation will be identified by the Warburg region curling towards the real axis of the Nyquist plot. This behavior indicates that the cathode is rate limited.

In previous studies, (003) LCO has shown no visible R_{CEI} semicircle in the pristine or postmortem state. However, Lu et al. use the typical circuit model for the EIS response of LCO to include the CEI contribution.[33] Furthermore, they assert that the active sites in (003) LCO are located where surface imperfections have occurred. Dai et al. found that Li diffusing facets (e.g. (101), (104)) LCO exhibit a two-semicircle impedance response, much like what is observed in composite cast electrodes. Dai et al. assign the higher frequency semicircle to the R_{CEI}.[17] The lower frequency semicircle is assigned to the R_{CT}.

As summarized in Fig. 4.1, EIS and confocal Raman spectroscopy can be used together to understand the how the electrochemical performance of different LTMO cathodes evolves during cycling. Our EIS results are fitted to reveal the interfacial changes that take place for each cathode. This interfacial characterization is complimented by the bulk information collected using confocal Raman images of postmortem cathodes.

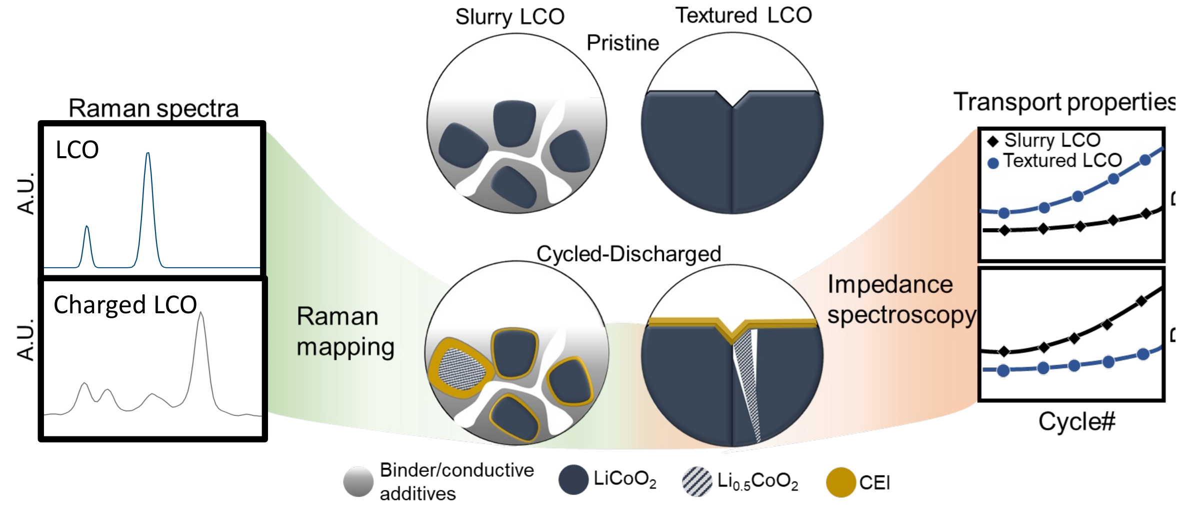

Figure 4.1. Overview of analysis of slurry-cast and textured LCO. Confocal Raman spectroscopy on cross-sectioned LCO reveals that after cycling, sections of both electrodes are in different states of charge. Intergranular cracks are observed occur after cycling throughout the bulk of the textured cathodes, which appears to reduce the fraction of the electrode participating in electrochemical cycling. In EIS, this is observed as an increase in the cathode R_{ct}. Interestingly R_{ct} increases more rapidly for the textured LCO, while R_{CEI} increases more rapidly for the slurry-cast LCO indicating the mechanisms for capacity fade in textured and particle-based cathodes may be different.

SEM images of the pristine cathode microstructure are shown in Fig. 4.2a-c. The microstructure of the pristine (003) LCO is composed of 20 µm thick grains aligned parallel to the substrate (Fig. 4.2a), while pristine (104) LCO consists of grains are up to 5 µm wide (Fig. 2c). The surface image of the pristine composite electrode shows LCO particles surrounded by binding material (Fig. 4.2e). Cross-sectional images shown in Fig. 4.2b, d, f, reveal that the textured electrodes are around 30 µm thick with grains that cross the majority of the electrode thickness, while cross-sections of the composite electrode show it is approximately 60 μm thick. These images show that each cathode is free of significant defects before electrochemical cycling. The theta-2 theta XRD plots for the textured LCO electrodes (Fig. 4.2g) qualitatively indicate the (003) and (104) electrodes are strongly textured.

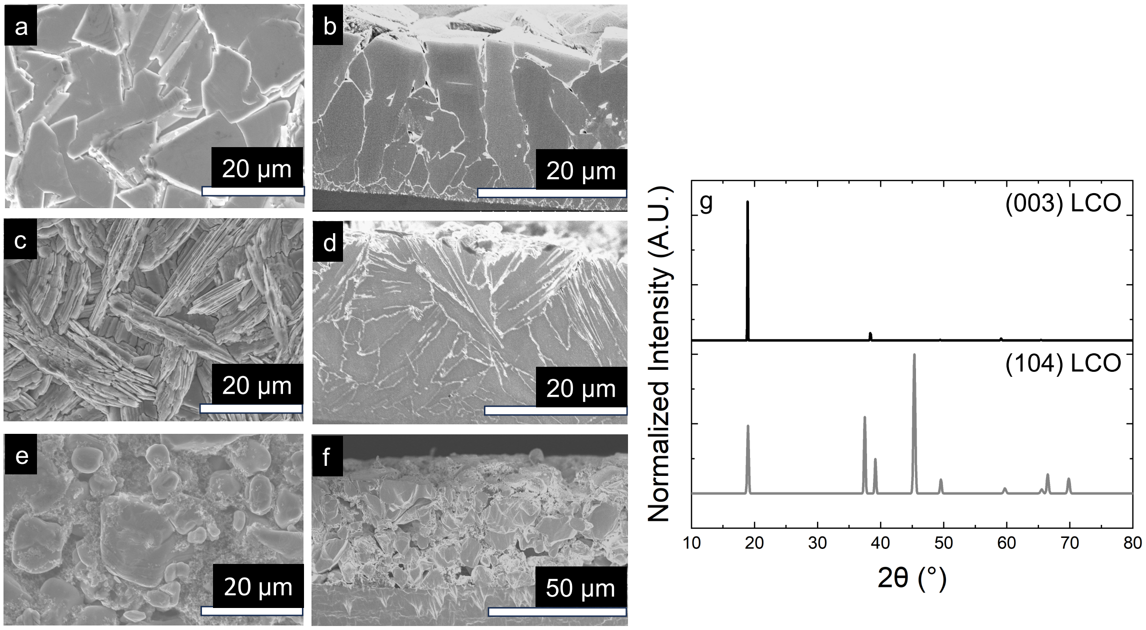

Figure 4.2. SEM and XRD of each cathode. a) SEM image of (003) LCO surface. The electrode surface is terminated by triangular platelets. b) SEM image of (003) LCO cross-section. c) SEM image of (104) LCO surface. The surface of this electrode is terminated by vertically aligned platelets. d) SEM image of pristine (104) LCO cross-section. e) SEM image of A-LCO surface. This electrode is comprised of primary and secondary particle aggregates. f) SEM image of A-LCO cross-section. g) XRD of (003) and (104) LCO. The most intense peak of a given electrode reflects the preferential orientation. The reference for each peak comes from the ICSD 51182 diffraction data for $LiCoO_2$.

4.2 Interfacial Characterization of Electrodeposited Lithium Cobalt Oxide using Electrochemical Impedance Spectroscopy

We used galvanostatic cycling with potential limitation (GCPL) to measure the half-cell capacity retention of each LCO cathode throughout its cycle life, as shown in Fig. 4.3a. The capacity retention of each electrode is measured at C/2 for 100 cycles. After 100 cycles, the capacity retention of the A-LCO is the highest at 67.9%, followed by (104) LCO at 65.9%. (003) LCO possesses the worst capacity retention after 100 cycles with 48.5%. We believe that the accumulation of strain during high-rate cycling induces crack formation in textured LCO electrodes, which leaves sections of the cathode in different states of charge.

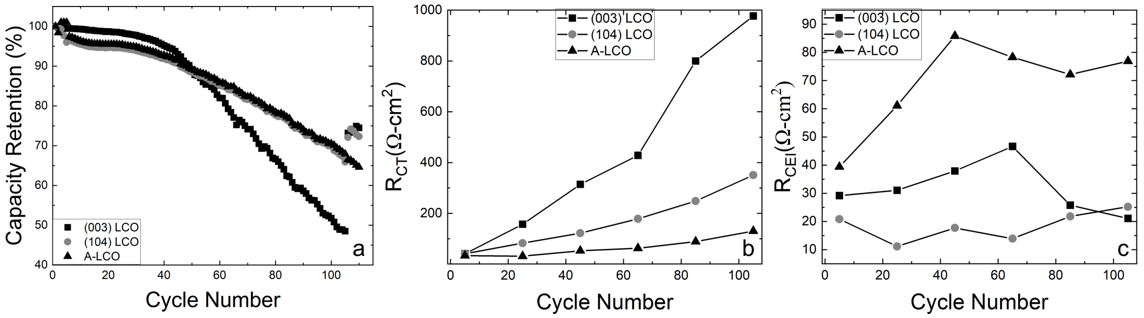

Figure 4.3. Half-cell Electrochemical Data Summary. EIS measurements were collected at 4.2 V (vs. Li/Li^+) for each electrode. a) Capacity retention vs. cycle number for each electrode. The cycles proceeding cycle 100 were completed at C/2, while cycles after cycle 100 were completed at C/15. b) R_{CT} vs. cycle number. R_{CT} growth is expected to be proportional to the extent of cathode cracking. c) R_{CEI} vs. cycle number. R_{CEI} increases as the thickness of the CEI grows.

The electrochemical impedance spectroscopy (EIS) results illustrated in Fig. 4.3b-c were collected to study how the impedance behavior of each cathode changes at 4.20 V (vs. Li/Li^+) as a function of cycle number. These spectra were collected every 20 cycles. As shown in Fig. 4.3b, R_{CT} vs. cycle number is plotted to compare the R_{CT} growth of each cathode. The results shown in Fig. 4.3b reflect that the R_{CT} of A-LCO, (003) LCO, and (104) LCO increase by 292%, 2280%, and 755% after 100 cycles, respectively. Cathode active area reduction has previously been demonstrated by measuring half-cell R_{CT} growth. We conclude that (003) LCO cracks severely reduce the active surface area of this cathode. The R_{CEI} data obtained for each cathode is included in Fig. 4.3c. The growth of a thick CEI adds an additional barrier for lithium diffusion and accelerates the process of electrolyte decomposition.[61], [62], [63] As illustrated in Fig. 4.3c, the A-LCO R_{CEI} grows by 95.33% during long-term GCPL. The A-LCO CEI growth is likely a drawback of the high porosity of this electrode (32.4%). We also observe that (104) LCO R_{CEI} only grows 7.62% in 100 cycles. (104) LCO has a low porosity (2.77%) which means area the CEI can grow on is lesser than the A-LCO cathode. The EIS results for (003) LCO indicate that the CEI resistance of this cathode reduces by 27.7% during its cycle life. However, it is important to mention that fitting this spectrum is rather difficult due to the overlap of the CEI and CT semicircles. We believe the CEI contribution to the total impedance observed in the (003) LCO cathode is insignificant in comparison to the R_{CT} contribution. The A-LCO EIS results demonstrate long-term capacity retention of A-LCO is negatively impacted by the concurrent growth of R_{CT} and R_{CEI}. A-LCO is less susceptible to the reduction of its active surface area in comparison to the textured cathodes; moreover, the high porosity provides a larger surface area for electrolyte decomposition than for a dense textured cathode. After cycling each half-cell at C/2 rate for 100 cycles, the cycling rate is reduced to C/15, as shown in Fig. 3a. After 10 cycles at C/15, the textured cathodes recover significant capacity as the capacity retention of (104) LCO and (003) LCO improve to 85.6% and 73.0%, respectively. We deduce that textured cathodes experience mass transfer limitation after long term cycling. In textured cathodes, lithium is able to diffuse into the bulk structure as the cycling rate is decreased. The A-LCO cathode capacity retention continues to degrade as the final retention after the C/15 cycling is 68.6%.

4.3 Bulk Characterization of Electrodeposited Lithium Cobalt Oxide using Confocal Raman Spectroscopy

Confocal Raman images of pristine LCO cathodes are useful to examine the bulk chemistry of LCO cathodes before cycling. Bright field images of pristine cathode cross-sections are shown in Fig. 4.4 (4.4a, 4.4d, and 4.4g). Samples of the spectra obtained in the following images are shown in Fig. A1. As previously stated, fully lithiated LCO is identified by the typical $A_{1g} + E_g$ response seen in LTMO materials.[52] Lithium deficient regions are identified by observing a four mode spectra which consist of 463 cm^{-1}, 508 cm^{-1}, 608 $cm^{-1,}$ and 670 cm^{-1} modes. An inconsistent intensity for the 590 cm^{-1} Raman mode throughout the thickness of the A-LCO cross-section is observed due to the presence of carbon, as shown in Fig. 4.4b. When the bright field image of A-LCO is examined, a strong 590 cm^{-1} mode is measured where individual LCO particles are present. The image of the 670 cm^{-1} Raman mode shown in Fig. 4.4c indicates that this mode is very weak across the pristine A-LCO cross-section, which indicates that the particles that comprise this electrode are lithium rich. The Raman images of the electroplated electrodes shown in Fig. 4.4e and Fig. 4.4h reveal that each pristine cathode is lithium rich before cycling as the 590 cm^{-1} signal is strong across the area scanned. From the 670 cm^{-1} images shown in Fig. 4.4f and Fig. 4.4i, we discern that the textured LCO is locally lithium deficient around some grain boundaries in the discharged state.

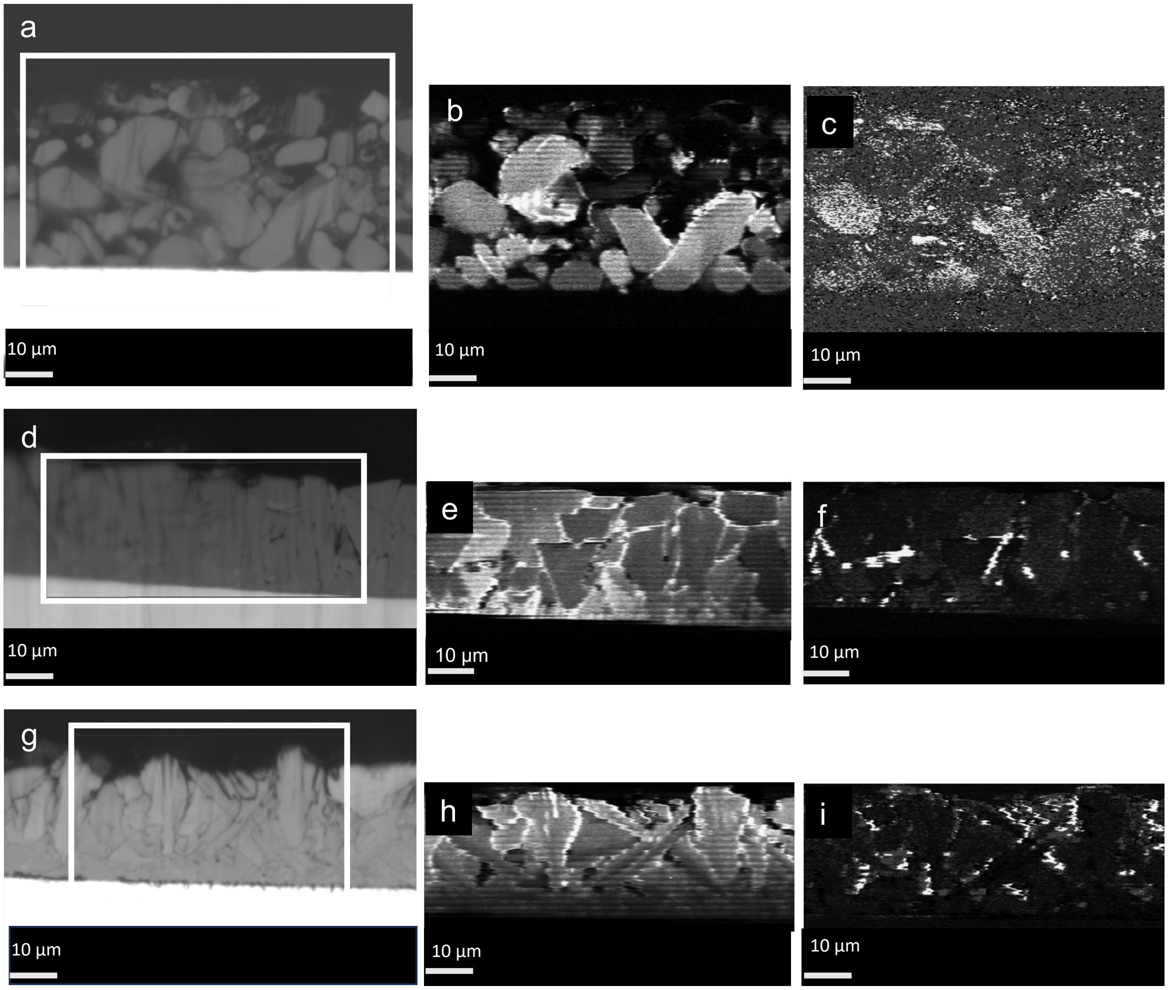

Figure 4.4. Raman Images of Pristine LCO. a) Bright field image of pristine A-LCO cross-section. b) 590 cm^{-1} Raman image of pristine A-LCO cross-section. c) 670 cm^{-1} Raman image of pristine A-LCO cross-section. d) Bright field image of (pristine 003) LCO cross-section. e) 590 cm^{-1} Raman image of pristine (003) LCO cross-section. f) 670 cm^{-1} Raman image of pristine (003) LCO cross-section. g) Bright field image of pristine (104) LCO cross-section. h) 590 cm^{-1} Raman image of pristine (104) LCO. i) 670 cm^{-1} Raman image of pristine (104) LCO.

Postmortem Raman images of A-LCO to were collected scan a commercially viable cathode for changes in bulk chemistry. Images of the postmortem A-LCO cathode, shown in Fig. 4.5 (a-c), reveal that LCO particles are in disparate states of charge after long-term electrochemical cycling. We highlight that intragranular cracks in these LCO particles are visible at high magnification, as shown in Fig. A3. These cracks can electrochemically isolate sections of LCO particles from the remainder of the cathode; however, as previously stated, examining the local chemistry of the cracked sections using SEM is difficult. As seen in Fig. 4.5b, it is clear that some regions of the cross-sectioned A-LCO cathode are in the discharged state, evidenced by their strong A_{1g} response (590 cm^{-1}). Observing the 670 cm^{-1} response, it is obvious that the remaining LCO in the cross-sectioned cathode was in the charged state prior to cell deconstruction (Fig. 4.5c). These Raman images indicate that intragranular particle cracking reduces the active mass of single crystalline LCO during long-term cycling. We anticipate that the degree of observed bulk heterogeneity will be greater for the electrodeposited LCO cathodes as stress accumulation in these cathodes should be more severe than what is observed for A-LCO given the size of the grains in these deposits.

To test this hypothesis, postmortem images of (003) LCO were collected, as shown in Fig. 4.5d-f. In the postmortem bright field image of (003) LCO, a large crack is seen across the imaged cross-section (Fig. 4.5d). The strongest 590 cm^{-1} signal in this image is detected near the substrate (Fig. 4.5e). Filtering the Raman data for the 670 cm^{-1} response (Fig. 4.5f) reveals that the majority of this cross section is in the charged state. It appears that these samples readily experience delamination during repeated cycling; moreover, this result confirms that (003) LCO loses the bulk of its active material during high-rate cycling. Since the 670 cm^{-1} Raman mode is detected at 4.2 V vs. Li/Li^+, we believe electrode fracture occurs as (003) LCO is de-lithiated to the upper voltage limit. This hypothesis is supported by the aforementioned growth in relative R_{CT} for (003) LCO. The Raman images reveal that bulk degradation is a significant contributor to the failure of (003) LCO. Examining additional Raman images of (003) LCO (Fig. A5), we find additional evidence of cracking across the (003) LCO cross-section. We discern that the disparate regions in this cross-section are tens of microns in size. These postmortem images further support the assertion that large cracks occur readily in LTMOs deposited in the direction normal to the (003) plane.[64] We conclude that cracks along the direction perpendicular to the current collector are detrimental for cathode performance. Therefore, we recommend avoiding fabricating next generation LTMOs with (003) oriented grains. We also captured images of postmortem (104) LCO to ascertain the impact of using a lithium facile LCO orientation in long-term electrochemical cycling. The postmortem bright field image of (104) (Fig. 4.5g) shows minimal evidence of cracking in this cross section. However, the 590 cm^{-1} Raman image in Fig. 4.5h reveals that highly lithiated regions are present in this cross-sectioned cathode. The remainder of the cathode is in the charged state, as detailed in Fig. 4.5i. These results suggest that, similarly to the other cathodes in this study, stress accumulation and release during electrochemical cycling leads to the formation of cracks in the bulk of the (104) LCO cathode. This cracking isolates regions of the electrode from participating in the insertion/extraction of lithium for to a lesser extent in (104) LCO in comparison to (003) LCO. The slow R_{CT} growth observed for (104) LCO is a result of its facile diffusion kinetics and stable CEI formation. These characteristics make this the superior texture to ensure long-term LIB cycle life in dense textured LTMO cathodes.

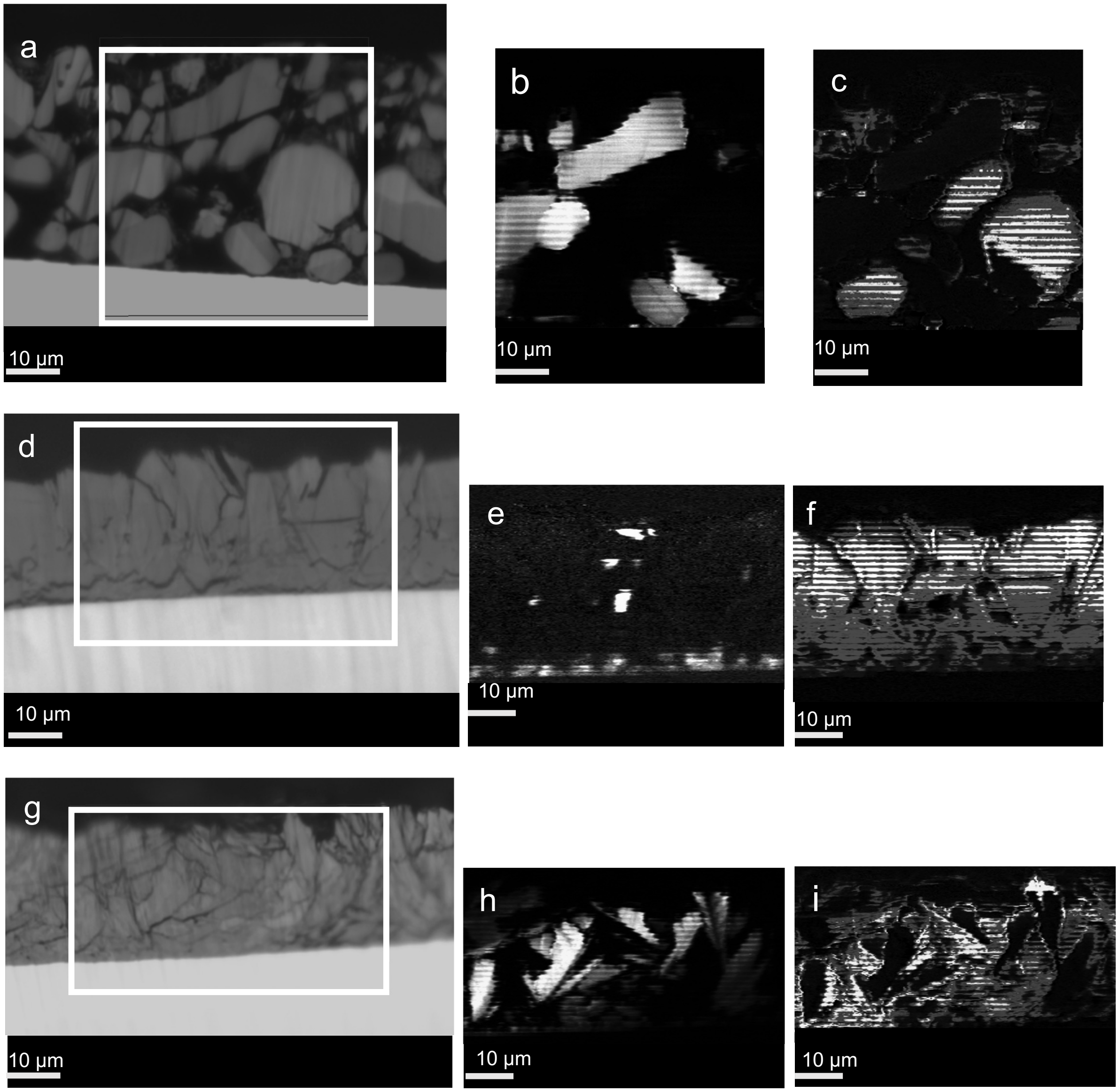

.

Figure 4.5. Postmortem confocal Raman spectroscopy on textured LCO summary. Each Raman image has been background subtracted. Cells were run at C/2 for 100 cycles. a) Postmortem bright field image of A-LCO. Cracks have randomly formed in individual LCO particles of the composite film. b) 590 cm^{-1} image of postmortem A-LCO. c: 670 cm^{-1} image of A-LCO. Individual particles of LCO in this film are in different states of charge. d) Postmortem bright field image of (003) LCO. e) Cross-sectional Raman image of postmortem (003) LCO at 590 cm^{-1}. f) 670 cm^{-1} Raman spectra of (003) LCO after 100 cycles @ C/2. The majority of the imaged area has lost its lithium content. g: Bright field image of postmortem (104) LCO cross-section. h) 590 cm^{-1} Raman image of (104) LCO after 100 cycles @ C/2. i) 670 cm^{-1} Raman spectra of (104) LCO after 100 cycles @ C/2. Some of the grains have retained their lithium content, while other grains have been electrochemically isolated from the film.

4.4 Conclusions

Preferentially oriented LCO cathodes were fabricated using electrodeposition. We cycled these cathodes to characterize their long-term stability, concurrently collecting EIS spectra to develop deeper insight about the changes that take place during cathode cycle life. It is determined that the resistance to charge transfer of a given cathode increases following electrochemical cycling, which indicates that the area of its charge transfer interface is decreasing. We support our conclusions on textured cathodes by baselining our results with the commercially viable slurry cast cathode, A-LCO. Our EIS results indicate that the main limitation of the A-LCO electrode is the growth of thick CEI. The relative R_{CT} results on A-LCO indicate that the charge transfer interface is stable during long term cycling. Amongst the electrodes included in this study, (104) LCO displays the best capacity retention (83.2%) at high cycle rates. We observe that R_{CT} growth in (104) electrodes is less rapid than for (003) electrodes at high cycling rates. Confocal Raman spectroscopy is used to detect the presence of degradation in the bulk of LTMO cathodes. These results are impactful, as insight on LTMO cracking is typically limited. The confocal Raman images of A-LCO illustrate that cracking is restricted to individual single crystals. It is apparent that the rate of R_{CT} growth of a given cathode can be limited by reducing active material cracking. Postmortem Raman images of the textured cathodes further support this conclusion. Postmortem confocal Raman images of (104) LCO confirm that charge heterogeneity is present in these cathodes, but that the extent of heterogeneity measured is less than what is seen for (003) LCO. Despite previous studies concluding that (003) LCO has great cycle stability in liquid electrolyte cells, we see cracks tens of microns in length in the direction perpendicular to the substrate for (003) LCO cathodes with high loading. These cracks are connected to the decrease in cell capacity as some LCO remains in the charged state and ceases participation in the charge transfer reaction during successive cycles. Moreover, these cracks severely reduce the area of the charge transfer interface, resulting in rapid R_{CT} growth for (003) LCO. The conclusions from this study are critical to the development of thick LTMO electrodes that can withstand degradation during long-term cycling. These results can be extended to influence the intelligent design of resilient single crystalline LTMO powders. Future research should be focused on synthesizing LTMO single crystals with high (104) surface area.

4.5 Experimental Methods

Electrochemical Experiments: The working electrodes used in this study were preferentially oriented $LiCoO_2$ and slurry casted single crystal $LiCoO_2$. The cells in this study were made using cathodes 8 mm in diameter. The preferentially oriented $LiCoO_2$ electrodes were obtained from Xerion Advanced Battery Corp. These 30 μm thick $LiCoO_2$ electrodes were electrodeposited onto stainless steel substrates. The majority of electrodeposited $LiCoO_2$ grains in (104) LCO are grown in the direction normal to the (104) plane. Similarly, (003) LCO is grown in the direction normal to the (003) plane. The composite cathode (A-C010A) used in this study was obtained from the Cell Analysis Modelling and Prototyping (CAMP) Facility at Argonne National Lab. We refer to this electrode as A-LCO. A-LCO is comprised of 94 wt% $LiCoO_2$, 2 wt% C45 carbon black, and 4 wt% Solvay 5130 polyvinylidene difluoride (PVDF) binder. This sample is composed of LCO single crystals with no preferred geometry. To study the long-term impedance behavior of each electrode, half cells were constructed using a lithium anode, Celgard 2325 separator, and 1 M $LiPF_6$ in EC/DMC (1:1 w/w). Galvanostatic charge/discharge cycling was conducted in the 3–4.20 V range at room temperature. Electrochemical impedance spectroscopy (EIS) was performed on half-cells every 20 cycles at 4.20 V (vs. Li/Li^+) to analyze the changes in the cathode electrolyte interphase (CEI) resistance and cathode resistance to charge transfer. An example fit for the EIS data is shown in Fig. A9. The rate ladder experiment was completed on half-cells of each texture. Following charging at a constant rate of C/5, discharge was completed at rates that changed in five cycle increments. To eliminate the effects of a lithium source on LCO Raman spectra[57], long-term cycling was conducted with full cells with a graphite based counter electrode (A-A015A). This electrode was provided by the CAMP facility. It consists of 91.83 wt% Superior Graphite, 2 wt% Timcal C45 carbon, 6 wt% PVDF binder, and 0.17% Oxalic acid. The N/P ratio of the textured electrodes used in this study was 1.13, while the N/P ratio of the composite cathode cell was 1.05. Five formation electrochemical cycles were performed at C/10 for each full cell (1 C defined as 140 mAh/g in the 3.00-4.20 V of LCO). Full cells were subsequently cycled for 100 times at a C/2 rate. Prior to charge cycles, cells were rested until current was lower than C/20 rate to give the electrode time to achieve homogeny. After cycling, postmortem cells were deconstructed and rinsed in DMC to remove residual electrolyte and polished for Raman imaging.

Scanning Electron Microscopy (SEM): The images were obtained with a Hitachi 4800 SEM. The voltage was set to 3 kV. Magnification was typically set to 2.50K.

X-Ray Diffraction (XRD) Studies: XRD data were collected using a Bruker D8 Advance at 45 kV and 40 mA current. The XRD data were collected every 0.01 2θ using a scan speed of 0.01 °/sec. The laser wavelength was $\mathrm{CuK}_{\propto}$=1.5406 Å. The total relative contribution of the (003) reflection to the total measured intensity.

Raman Measurements: Postmortem cathodes were cut into cross sections using sharp scissors, mounted to a titanium polishing blade, and polished. Cross-sectional samples were polished using Gatan PECS II. The samples were polished with an 8 kV beam for 5 hours using single beam modulation. After polishing, Raman measurements were collected using a Witec AFM-Raman Microscope. The objective of the Witec Raman system was set to 50X magnification. The numerical aperture of the objective is 0.9. The resolution of the objective is 590 nm. The laser wavelength was set to 532 nm. The beam power was set to 0.8 mW during imaging. Using a power meter, the beam power at the sample was measured at 0.0032 mW. Raman images were constructed using 62,500 pixels.

CHAPTER 5: CYCLE LIFE STUDIES OF SINGLE CRYSTALLINE NICKEL RICH LITHIUM NICKEL MANGANESE COBALT OXIDES

5.1 Introduction and Motivation

In **Chapter 1**, the importance of reducing the cobalt content of LTMO materials was discussed. The primary driver for this reduction is the cost associated with the artisanal mining of cobalt, as well as the socioeconomic impact of this mining on relatively cobalt rich countries like the Democratic Republic of the Congo. As a result, candidates for next generation cathode materials include little to no cobalt (e.g. high voltage NMC/NCA, $LiNiO_2$).[6] This need has led researchers to attempt to increase our understanding on how to properly engineer NRCMs.

We discussed molten salt synthesis as a powerful tool for fabricating well faceted single crystalline NMC 811. We also discussed, various observations on the electrochemical properties of NMC single crystals terminated with (001), (012), and (104) facets. We understand that the high surface energy of (012)-dominant single crystals should lead to the development of a thick, resistive CEI. On the other hand, we believe the low surface energy and structure of (104)-dominant NMC make this facet an attractive option to maximize NRCM performance. We believe the results from studying these materials can tell us much about how to tailor the electrochemical properties of NRCMs as a class of materials.

We must consider the impact that tailoring the geometry of single crystalline NRCMs can have on the mechanical stability of a LIB cathode. In a typical LTMO material, there are anisotropic volume changes associated with charge/discharge. For NMC, the volume change measured is correlated to the content of transition metals in a crystal.[65]

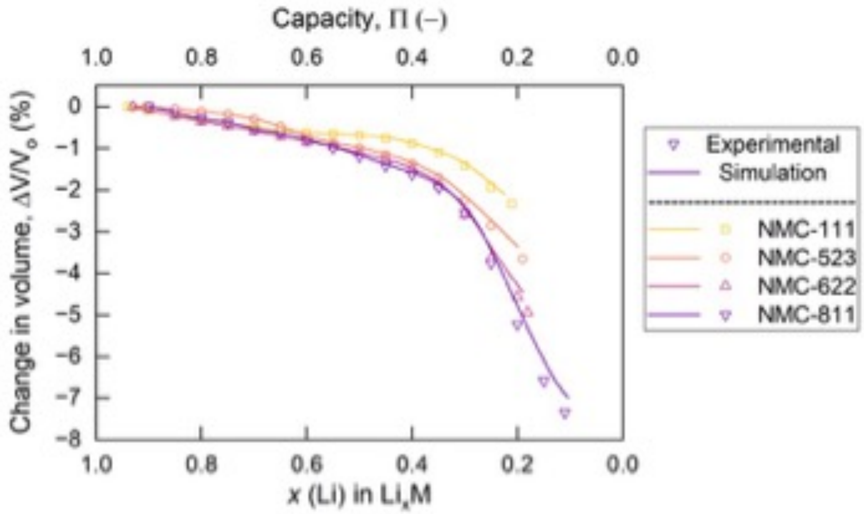

Figure 5.1: Volume changes measured for NMC as a function of transition metal and lithium content. As the nickel content increases, the maximum volume reduction increases (Reproduced from [65]).

In Figure 5.1, we show that the maximum volume reduction for NMC (at 100% state of charge) is proportional to the nickel content of this class of materials. This perspective is accurate for polycrystalline NMC, but we must also contextualize how the mechanical integrity of this material depends on the crystalline facet that is being studied, as we seek to unveil the dependence of NRCM cycle stability on the facets grown during synthesis. For NMC 622, the obtained results are summarized in Fig. 5.2.[29]

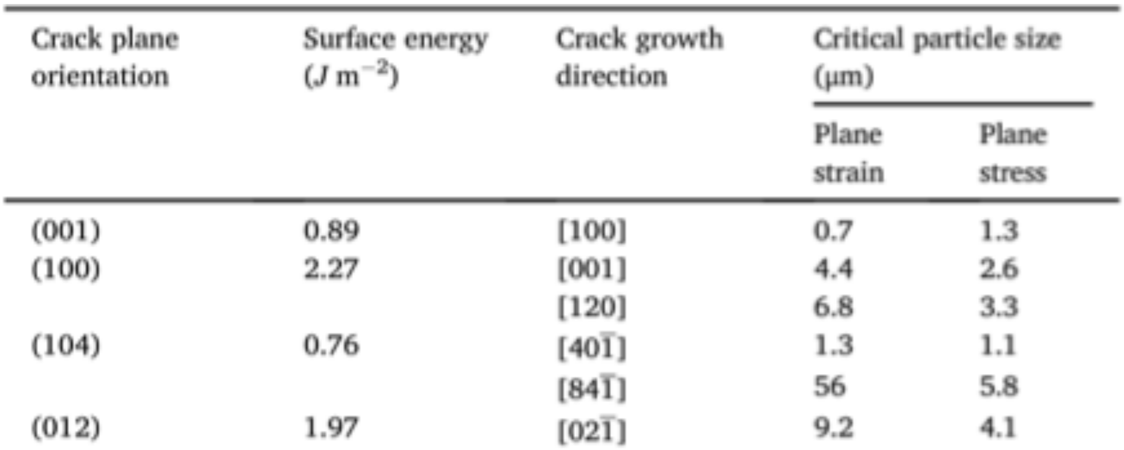

Crack plane orientation	Surface energy ($J\ m^{-2}$)	Crack growth direction	Critical particle size (μm)	
			Plane strain	Plane stress
(001)	0.89	[100]	0.7	1.3
(100)	2.27	[001]	4.4	2.6
		[120]	6.8	3.3
(104)	0.76	$[40\bar{1}]$	1.3	1.1
		$[84\bar{1}]$	56	5.8
(012)	1.97	$[02\bar{1}]$	9.2	4.1

Figure 5.2: Impact of crack plane orientation on critical particle size for NMC 622. It is apparent that the use of NMC single crystals with (001) surface termination limits the useable particle size for this class of material. (Reproduced from [29]).

In Fig. 5.2, we see that the (001) facet is the primary plane for crack propagation in NMC 622. This result is important because this limitation should also be true for more nickel rich NMC crystals. We expect that single crystals grown above the micron scale with (001) surface termination will be susceptible to intragranular fracture, which will then limit the long-term capacity of the battery. An additional issue caused by the development of particle fracture in single crystals is the exposure for new surfaces for electrolyte decomposition. CEI will then grow on these freshly exposed surfaces.

In this chapter, we seek to reveal whether the limitations associated with a given morphology of NMC 811 single crystals are detectable using EIS. Our goal is to accomplish this by studying the growth of R_{CEI} and R_{CT} over the duration of half-cell cycling.

5.2 Interfacial Characterization of NMC 811

We illustrated that we can obtain NMC 811 with low cation mixing in Chapter 3. Similarly to what we discussed in Chapter 4, we analyzed the interfacial behavior of the three different morphologies of NMC 811 that we obtained. Our results for this study are shown in Fig 5.3.

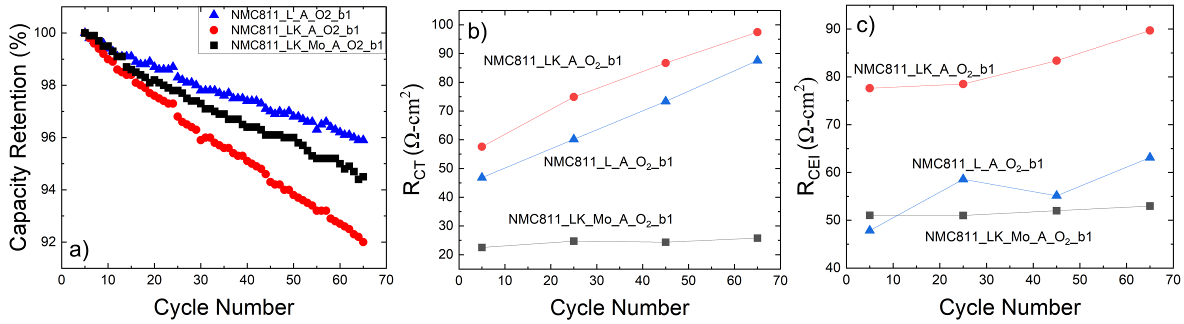

Figure 5.3: Half-cell Electrochemical Data Summary. EIS measurements were collected at 4.2 V (vs. Li/Li^+) for each electrode. a) Capacity retention vs. cycle number for each electrode. The cycles starting with cycle 5 were completed at C/2, while cycles proceeding cycle 5 were completed at C/10. b) R_{CT} vs. cycle number. R_{CT} growth is expected to be inversely proportional to the extent of active surface area remaining a particular cathode. c) R_{CEI} vs. cycle number. R_{CEI} increases as the thickness of the CEI grows.

As shown in Fig 5.3, the three cathodes that we fabricated have noticeably different capacity retention, R_{CEI}, and R_{CT} as a function of the cycle number. We observe in Fig. 5.3a that NMC811_L_O_2_b1 retains the highest capacity retention after 65 cycles, followed by NMC811_LK_Mo_O_2_b1, and NMC811_LK_A_O_2_b1, respectively. It is important to note the extent to which the discharge capacity changes during this cycling. Initially, the capacity of NMC811_LK_Mo_O_2_b1 is 187.44 mAh/g. The final discharge capacity value for this cathode is 176.65 mAh/g. For NMC811_LK_O_2_b1, the initial capacity is 182.31 mAh/g, while the final discharge capacity is 167.68 mAh/g. Finally, the initial discharge capacity value of NMC811_L_O_2_b1 178.81 mAh/g, while the final discharge capacity value is 171.41 mAh/g. Only relying on this data and the morphology of the cathode is insufficient in detailing why a given cathode has a certain capacity retention after a given number of cycles. We look to use EIS to characterize how the interfacial behavior influences the degree of capacity fade that we observe.

As mentioned in Chapter 3, each of the flux compositions we used influenced the growth of different single crystal morphologies. The EIS results depicted in Fig 5.3b-c, reflect that each cathode experiences different R_{CT} and R_{CEI} changes during long-term cycling. The RCT growth is the most dramatic for NMC811_LK_A_O_2_b1. More specifically, R_{CT} grows 69.4% for NMC811_LK_A_O_2_b1 in 65 cycles, while NMC811_LK_Mo_O_2_b1 and NMC811_L_O_2_b1 grow 14.5% and 87.1%, respectively. We detailed in Chapter 4 that the R_{CT} is inversely proportional to the electroactive surface area of a given cathode. Using this knowledge, we can infer that NMC811_LK_A_O_2_b1 has the smallest electroactive surface area proceeding electrochemical cycling and this area reduces to a further extent following long-term cycling. On the other hand, it is apparent that the addition of Mo to NMC811_LK_Mo_O_2_b1 increases the electroactive surface area of this material, perhaps by promoting the termination of the NMC surface with (104) facets. Moreover, the R_{CT} of this cathode remains the most stable following 65 cycles.

In Fig. 5.3c, the R_{CEI} for each sample is shown as a function of cycle number. Again, we find that the CEI resistance of NMC811_LK_Mo_O_2_b1 remains the most stable amongst the cathodes we included for this study during long-term cycling, since the R_{CEI} only grows 3.82% in 65 cycles. This result makes sense as the (104) facet of NMC 811 has the lowest surface energy of the equilibrium facets. Interestingly, R_{CEI} of NMC811_LK_O_2_b1 is the highest initially (77.6 Ω-cm^2), despite the inclusion of (001) facets which are not susceptible to electrolyte decomposition. Furthermore, the R_{CEI} value for this cathode is the highest following electrochemical cycling (89.7 Ω-cm^2). If we look at the percentage of R_{CEI} growth for each cathode, we observe that the R_{CEI} value for NMC811_L_A_O2_b1 to increases at a slower rate (15.6% in 65 cycles) than NMC811_LK_O_2_b1 (31.9% in 65 cycles) during its cycle life. This result makes sense as the (012) facet is the most prominent facet for electrolyte decomposition due to its inherently high surface energy.

5.3 Conclusions

In this chapter, we characterized the interfacial changes that take place in NMC 811 during long-term electrochemical cycling. We find that maximizing the (104) surface area of NMC 811 is beneficial in promoting stable interfacial properties and maximizing the discharge capacity of this class of materials during high-rate cycling. We also find that NMC 811 single crystals with exposed (001) facets suffer from more severe capacity fade during high-rate cycling than single crystals with predominantly active surface facets. We believe that mechanical degradation of NMC 811 crystals exposes new surfaces for electrolyte decomposition to continue. Overall, our results indicate that maximizing the (104) surface area for NRCMs can reduce the overall capacity fade experienced by this family of cathode materials.

5.4 Experimental Methods

Electrochemical Measurements: The working electrodes used in this study were NMC 811 single crystals, which were synthesized as described in **Chapter 3, section 3.6**. These crystals were formed into cathode films by Rajen Basu, who fabricated cathodes using 87% single crystalline NMC 811, 6% PVDF, and 7% carbon black. The half-cells in this study were made using cathodes 10 mm in diameter. The long-term impedance behavior of each NMC 811 electrode was studied using half cells consisting of a NMC 811 cathode, lithium anode, Celgard 2325 separator, and 1 M $LiPF_6$ in EC/DMC (1:1 w/w). Galvanostatic charge/discharge cycling was conducted in the 3–4.20 V range at room temperature. Starting at cycle 5, electrochemical impedance spectroscopy (EIS) was performed on half-cells every 20 cycles at 4.30 V (vs. Li/Li^+) to analyze the changes in the cathode electrolyte interphase (CEI) resistance and cathode resistance to charge transfer as a function of the cycle number.

CHAPTER 6: SUMMARY OF WORK AND FUTURE DIRECTIONS

6.1 Summary of Work

In this work, we detailed how preferential orientation influences the electrochemical aging of LTMO materials from the perspectives of the interfacial and bulk changes that take place during cycling. First, we introduced LIBs and the fundamental limitations of LTMO cathode materials in **Chapter 1**. Then, we discussed our electrodeposition process in **Chapter 2**, followed by outlining the molten salt synthesis procedure in **Chapter 3**. After, we went into great detail of how we analyzed preferentially oriented electrodeposited LCO cathodes using EIS and confocal Raman spectroscopy in **Chapter 4**. The insights on the impact of preferential orientation and the benefit of maximizing the (104) surface area of active materials was applied to the fabrication of the NRCM NMC 811. We used our insights to characterize the interfacial behavior of three distinct NMC 811 morphologies in **Chapter 5**.

Overall, we found that maximizing the exposed (104) surface area of LTMO materials maximizes the interfacial stability of these materials and increases the viability of specific LMTOs like NRCMs for long-term electrochemical cycling. We also found that molten salt synthesis is a useful technique for achieving low cation mixing in NRCMs in air under controlled synthesis conditions with specific precursors. These results are imperative for the development of next generation LTMO cathode materials with long cycle life.

6.2 Future Work

Our study on NMC 811 single crystals was limited to examining the interfacial changes that take place during electrochemical cycling. As we detailed for LCO, this approach is useful for describing the interfacial contributions to capacity fade in LTMO materials, but it is necessary to perform additional experiments to describe changes that take place in the bulk of these materials. We used confocal Raman spectroscopy to examine the bulk behavior of LCO. We believe that applying this technique to our NMC 811 single crystals will allow us to understand how the morphology of our crystals influences their bulk degradation. We believe that NMC811_LK_A_O_2_b1 crystals will experience a greater degree of bulk cracking than our other two single crystal morphologies. The biggest challenge we face in completing this task is fabricating a capacity matched anode to ensure that the full cells needed have the proper N/P ratio.

Another relevant topic for the development of NRCMs is the use of chemo-mechanical description to detail how the chemical and mechanical changes that take place during electrochemical cycling influence the aging of these materials.[66] Chemo-mechanical stress induced phase transition has been observed on NRCMs using TEM. In this study, it was observed that changes that take place during cycling, such as nickel reduction, influence the mechanical degradation of NRCMs. However, one limitation of this study is that this understanding was not applied to preferentially oriented NRCMs. We believe that the chemo-mechanical issues observed should depend on the crystal facet of the NRCM being examined. We suggest introducing this concept to single crystalline NRCMs like NMC 811 where there are large surfaces available for imaging. The understanding obtained from this study would allow researchers to further extend the cycle life of these materials.

REFERENCES

[1] G. Berckmans, M. Messagie, J. Smekens, N. Omar, L. Vanhaverbeke, and J. Van Mierlo, “Cost Projection of State of the Art Lithium-Ion Batteries for Electric Vehicles Up to 2030,” *Energies*, vol. 10, no. 9, Art. no. 9, Sep. 2017, doi: 10.3390/en10091314.

[2] M. Li, J. Lu, Z. Chen, and K. Amine, “30 Years of Lithium-Ion Batteries,” *Adv. Mater.*, vol. 30, no. 33, p. 1800561, 2018, doi: 10.1002/adma.201800561.

[3] N. Mohamed and N. K. Allam, “Recent advances in the design of cathode materials for Li-ion batteries,” *RSC Adv.*, vol. 10, no. 37, pp. 21662–21685, 2020, doi: 10.1039/D0RA03314F.

[4] E. M. Erickson *et al.*, “Review—Recent Advances and Remaining Challenges for Lithium Ion Battery Cathodes: II. Lithium-Rich, $xLi_2MnO_3 \cdot (1-x)LiNi_aCo_bMn_cO_2$,” *J. Electrochem. Soc.*, vol. 164, no. 1, pp. A6341–A6348, 2017, doi: 10.1149/2.0461701jes.

[5] B. Wu, C. Chen, D. L. Danilov, R.-A. Eichel, and P. H. L. Notten, “All-Solid-State Thin Film Li-Ion Batteries: New Challenges, New Materials, and New Designs,” *Batteries*, vol. 9, no. 3, Art. no. 3, Mar. 2023, doi: 10.3390/batteries9030186.

[6] W. Li, E. M. Erickson, and A. Manthiram, “High-nickel layered oxide cathodes for lithium-based automotive batteries,” *Nat. Energy*, vol. 5, no. 1, Art. no. 1, Jan. 2020, doi: 10.1038/s41560-019-0513-0.

[7] J.-M. Kim, X. Zhang, J.-G. Zhang, A. Manthiram, Y. S. Meng, and W. Xu, “A review on the stability and surface modification of layered transition-metal oxide cathodes,” *Mater. Today*, vol. 46, pp. 155–182, Jun. 2021, doi: 10.1016/j.mattod.2020.12.017.

[8] C. Yang *et al.*, “Bulk and surface degradation in layered Ni-rich cathode for Li ions batteries: Defect proliferation via chain reaction mechanism,” *Energy Storage Mater.*, vol. 35, p. 62, Nov. 2020, doi: 10.1016/j.ensm.2020.11.016.

[9] G. Sun *et al.*, “Synergistic effects of ion doping and surface-modifying for lithium transition-metal oxide: Synthesis and characterization of La2O3-modified LiNi1/3Co1/3Mn1/3O2,” *Electrochimica Acta*, vol. 272, pp. 11–21, May 2018, doi: 10.1016/j.electacta.2018.03.175.

[10] K.-J. Park, H.-G. Jung, L.-Y. Kuo, P. Kaghazchi, C. S. Yoon, and Y.-K. Sun, “Improved Cycling Stability of $Li[Ni_{0.90}Co_{0.05}Mn_{0.05}]O_2$ Through Microstructure Modification by Boron Doping for Li-Ion Batteries,” *Adv. Energy Mater.*, vol. 8, no. 25, p. 1801202, Sep. 2018, doi: 10.1002/aenm.201801202.

[11] S. Krishna Kumar, S. Ghosh, and S. K. Martha, “Synergistic effect of magnesium and fluorine doping on the electrochemical performance of lithium-manganese rich (LMR)-based Ni-Mn-Co-oxide (NMC) cathodes for lithium-ion batteries,” *Ionics*, vol. 23, no. 7, pp. 1655–1662, Jul. 2017, doi: 10.1007/s11581-017-2018-9.

[12] B. Xiao and X. Sun, “Surface and Subsurface Reactions of Lithium Transition Metal Oxide Cathode Materials: An Overview of the Fundamental Origins and Remedying Approaches,” *Adv. Energy Mater.*, vol. 8, no. 29, p. 1802057, 2018, doi: 10.1002/aenm.201802057.

[13] Z. Duan, Y. Wu, J. Lin, L. Wang, and D.-L. Peng, “Thin-Film Lithium Cobalt Oxide for Lithium-Ion Batteries,” *Energies*, vol. 15, no. 23, Art. no. 23, Jan. 2022, doi: 10.3390/en15238980.

[14] C. M. Julien, A. Mauger, and O. M. Hussain, “Sputtered LiCoO2 Cathode Materials for All-Solid-State Thin-Film Lithium Microbatteries,” *Materials*, vol. 12, no. 17, Art. no. 17, Jan. 2019, doi: 10.3390/ma12172687.

[15] B. Wang, J. B. Bates, F. X. Hart, B. C. Sales, R. A. Zuhr, and J. D. Robertson, "Characterization of Thin-Film Rechargeable Lithium Batteries with Lithium Cobalt Oxide Cathodes," *J. Electrochem. Soc.*, vol. 143, no. 10, p. 3203, Oct. 1996, doi: 10.1149/1.1837188.

[16] P. J. Bouwman, B. A. Boukamp, H. J. M. Bouwmeester, and P. H. L. Notten, "Influence of Diffusion Plane Orientation on Electrochemical Properties of Thin Film LiCoO2 Electrodes," *J. Electrochem. Soc.* vol. 149, no. 6, p. A699-A709, Apr. 2002, doi: 10.1149/1.1471543.

[17] X. Dai *et al.*, "Controllable preparation and electrochemical properties of In-situ annealed LiCoO2 films with a specific crystalline orientation on stainless steel substrates," *Solid State Ion.*, vol. 365, p. 115658, Jul. 2021, doi: 10.1016/j.ssi.2021.115658.

[18] J. Xie, N. Imanishi, T. Matsumura, A. Hirano, Y. Takeda, and O. Yamamoto, "Orientation dependence of Li–ion diffusion kinetics in LiCoO2 thin films prepared by RF magnetron sputtering," *Solid State Ion.*, vol. 179, no. 9, pp. 362–370, May 2008, doi: 10.1016/j.ssi.2008.02.051.

[19] H. Zhang *et al.*, "Electroplating lithium transition metal oxides," *Sci. Adv.*, vol. 3, no. 5, p. e1602427, May 2017, doi: 10.1126/sciadv.1602427.

[20] B. You *et al.*, "Research Progress of Single-Crystal Nickel-Rich Cathode Materials for Lithium Ion Batteries," *Small Methods*, vol. 5, no. 8, p. 2100234, 2021, doi: 10.1002/smtd.202100234.

[21] "Heuristics for Molten-Salt Synthesis of Single-Crystalline Ultrahigh-Nickel Layered Oxide Cathodes." Accessed: Jul. 26, 2023. [Online]. Available: https://pubs.acs.org/doi/epdf/10.1021/acsami.2c16326

[22] A. J. Bard, L. R. Faulkner, and H. S. White, *Electrochemical Methods: Fundamentals and Applications*. John Wiley & Sons, 2022.

[23] G. Ding *et al.*, "Molten Salt-Assisted Synthesis of Single-Crystalline Nonstoichiometric Li1+xNi1–xO2 with Improved Structural Stability," *Adv. Energy Mater.*, vol. 13, no. 23, p. 2300407, 2023, doi: 10.1002/aenm.202300407.

[24] T. Kimijima, N. Zettsu, and K. Teshima, "Growth Manner of Octahedral-Shaped Li(Ni1/3Co1/3Mn1/3)O2 Single Crystals in Molten Na2SO4," *Cryst. Growth Des.*, vol. 16, no. 5, pp. 2618–2623, May 2016, doi: 10.1021/acs.cgd.5b01723.

[25] J. Langdon and A. Manthiram, "A perspective on single-crystal layered oxide cathodes for lithium-ion batteries," *Energy Storage Mater.*, vol. 37, pp. 143–160, May 2021, doi: 10.1016/j.ensm.2021.02.003.

[26] J. Zhu and G. Chen, "Single-crystal based studies for correlating the properties and high-voltage performance of Li[Ni x Mn y Co 1−x−y]O 2 cathodes," *J. Mater. Chem. A*, vol. 7, no. 10, pp. 5463–5474, 2019, doi: 10.1039/C8TA10329A.

[27] A. Mesnier and A. Manthiram, "Heuristics for Molten-Salt Synthesis of Single-Crystalline Ultrahigh-Nickel Layered Oxide Cathodes," *ACS Appl. Mater. Interfaces*, vol. 15, no. 10, pp. 12895–12907, Mar. 2023, doi: 10.1021/acsami.2c16326.

[28] E. D. Orlova, A. A. Savina, S. A. Abakumov, A. V. Morozov, and A. M. Abakumov, "Comprehensive Study of Li+/Ni2+ Disorder in Ni-Rich NMCs Cathodes for Li-Ion Batteries," *Symmetry*, vol. 13, no. 9, Art. no. 9, Sep. 2021, doi: 10.3390/sym13091628.

[29] G. Qian *et al.*, "Single-crystal nickel-rich layered-oxide battery cathode materials: synthesis, electrochemistry, and intra-granular fracture," *Energy Storage Mater.*, vol. 27, pp. 140–149, May 2020, doi: 10.1016/j.ensm.2020.01.027.

[30] P. Teichert, G. G. Eshetu, H. Jahnke, and E. Figgemeier, “Degradation and Aging Routes of Ni-Rich Cathode Based Li-Ion Batteries,” *Batteries*, vol. 6, no. 1, Art. no. 1, Mar. 2020, doi: 10.3390/batteries6010008.

[31] I. A. Moiseev *et al.*, “Single crystal Ni-rich NMC cathode materials for lithium-ion batteries with ultra-high volumetric energy density,” *Energy Adv.*, vol. 1, no. 10, pp. 677–681, 2022, doi: 10.1039/D2YA00211F.

[32] Z. Wu *et al.*, “Improving electrochemical performance of NCM811 cathodes for lithium-ion batteries via consistently arranging the hexagonal nanosheets with exposed {104} facets,” *Ceram. Int.*, vol. 48, no. 12, pp. 17279–17288, Jun. 2022, doi: 10.1016/j.ceramint.2022.02.289.

[33] W. Lu, J. Zhang, J. Xu, X. Wu, and L. Chen, “In Situ Visualized Cathode Electrolyte Interphase on $LiCoO_2$ in High Voltage Cycling,” *ACS Appl. Mater. Interfaces*, vol. 9, no. 22, pp. 19313–19318, Jun. 2017, doi: 10.1021/acsami.7b03024.

[34] Y. Kim, “Lithium Nickel Cobalt Manganese Oxide Synthesized Using Alkali Chloride Flux: Morphology and Performance As a Cathode Material for Lithium Ion Batteries,” *ACS Appl. Mater. Interfaces*, vol. 4, no. 5, pp. 2329–2333, May 2012, doi: 10.1021/am300386j.

[35] H. Huang, H. Zhu, J. Gao, J. Wang, M. Shao, and W. Zhou, “Grain-growth Inhibitor with Three-section-sintering for Highly Dispersed Single-crystal NCM90 Cubes,” *Angew. Chem. Int. Ed.*, vol. 63, no. 2, p. e202314457, 2024, doi: 10.1002/anie.202314457.

[36] B.-S. Lee *et al.*, “Analysis of Rate-Limiting Factors in Thick Electrodes for Electric Vehicle Applications,” *J. Electrochem. Soc.*, vol. 165, no. 3, p. A525, Feb. 2018, doi: 10.1149/2.0571803jes.

[37] D. Beck, P. Dechent, M. Junker, D. U. Sauer, and M. Dubarry, “Inhomogeneities and Cell-to-Cell Variations in Lithium-Ion Batteries, a Review,” *Energies*, vol. 14, no. 11, Art. no. 11, Jan. 2021, doi: 10.3390/en14113276.

[38] D. Li *et al.*, “The Effect of Electrode Thickness on the High-Current Discharge and Long-Term Cycle Performance of a Lithium-Ion Battery,” *Batteries*, vol. 8, no. 8, Art. no. 8, Aug. 2022, doi: 10.3390/batteries8080101.

[39] H. Wang, Y. Jang, B. Huang, D. R. Sadoway, and Y. Chiang, “TEM Study of Electrochemical Cycling-Induced Damage and Disorder in LiCoO2 Cathodes for Rechargeable Lithium Batteries,” *J. Electrochem. Soc.*, vol. 146, no. 2, pp. 473–480, Feb. 1999, doi: 10.1149/1.1391631.

[40] P. Bouwman, “Structure-related intercalation behaviour of LiCoO2 films,” *Solid State Ion.*, vol. 152–153, pp. 181–188, Dec. 2002, doi: 10.1016/S0167-2738(02)00298-9.

[41] J. A. Gilbert *et al.*, “Cycling Behavior of NCM523/Graphite Lithium-Ion Cells in the 3–4.4 V Range: Diagnostic Studies of Full Cells and Harvested Electrodes,” *J. Electrochem. Soc.*, vol. 164, no. 1, pp. A6054–A6065, 2017, doi: 10.1149/2.0081701jes.

[42] M. Börner *et al.*, “Degradation effects on the surface of commercial LiNi0.5Co0.2Mn0.3O2 electrodes,” *J. Power Sources*, vol. 335, pp. 45–55, Dec. 2016, doi: 10.1016/j.jpowsour.2016.09.071.

[43] A. M. Andersson, D. P. Abraham, R. Haasch, S. MacLaren, J. Liu, and K. Amine, “Surface Characterization of Electrodes from High Power Lithium-Ion Batteries,” *J. Electrochem. Soc.*, vol. 149, no. 10, p. A1358, 2002, doi: 10.1149/1.1505636.

[44] B. Lu, C. Ning, D. Shi, Y. Zhao, and J. Zhang, “Review on electrode-level fracture in lithium-ion batteries*,” *Chin. Phys. B*, vol. 29, no. 2, p. 026201, Feb. 2020, doi: 10.1088/1674-1056/ab6841.

[45] T. Ohzuku and A. Ueda, “Solid-State Redox Reactions of LiCoO2 (R3m) for 4 Volt Secondary Lithium Cells,” *J. Electrochem. Soc.*, vol. 141, no. 11, pp. 2972–2977, Nov. 1994, doi: 10.1149/1.2059267.

[46] G. G. Amatucci, J. M. Tarascon, and L. C. Klein, “CoO2, The End Member of the Li x CoO2 Solid Solution,” *J. Electrochem. Soc.*, vol. 143, no. 3, pp. 1114–1123, Mar. 1996, doi: 10.1149/1.1836594.

[47] G. Amatucci, “Cobalt dissolution in LiCoO2-based non-aqueous rechargeable batteries,” *Solid State Ion.*, vol. 83, no. 1–2, pp. 167–173, Jan. 1996, doi: 10.1016/0167-2738(95)00231-6.

[48] K. Funayama, T. Nakamura, N. Kuwata, J. Kawamura, T. Kawada, and K. Amezawa, “Electromotive force measurements of LiCoO2 electrode on a lithium ion-conducting glass ceramics under mechanical stress,” *Solid State Ion.*, vol. 285, pp. 75–78, Feb. 2016, doi: 10.1016/j.ssi.2015.09.009.

[49] Y. J. Kim *et al.*, “Changes in the Lattice Constants of Thin-Film LiCoO2 Cathodes at the 4.2 V Charged State,” *J. Electrochem. Soc.,* vol. 154, no. 7, pp A1063, June 2004, doi: 10.1149/1.1759611.

[50] L. Feng, X. Lu, T. Zhao, and S. Dillon, “The effect of electrochemical cycling on the strength of $LiCoO_2$,” *J. Am. Ceram. Soc.*, vol. 102, no. 1, pp. 372–381, Jan. 2019, doi: 10.1111/jace.15893.

[51] L. Wu and J. Zhang, “*Ab initio* study of anisotropic mechanical properties of $LiCoO_2$ during lithium intercalation and deintercalation process,” *J. Appl. Phys.*, vol. 118, no. 22, p. 225101, Dec. 2015, doi: 10.1063/1.4937409.

[52] Y. Matsuda, N. Kuwata, T. Okawa, A. Dorai, O. Kamishima, and J. Kawamura, “In situ Raman spectroscopy of Li CoO2 cathode in Li/Li3PO4/LiCoO2 all-solid-state thin-film lithium battery,” *Solid State Ion.*, vol. 335, pp. 7–14, Jul. 2019, doi: 10.1016/j.ssi.2019.02.010.

[53] J. A. Gilbert, V. A. Maroni, Y. Cui, D. J. Gosztola, D. J. Miller, and D. P. Abraham, “Composition and Impedance Heterogeneity in Oxide Electrode Cross-Sections Detected by Raman Spectroscopy,” *Adv. Mater. Interfaces*, vol. 5, no. 9, p. 1701447, May 2018, doi: 10.1002/admi.201701447.

[54] R. Baddour-Hadjean and J.-P. Pereira-Ramos, “Raman Microspectrometry Applied to the Study of Electrode Materials for Lithium Batteries,” *Chem. Rev.*, vol. 110, no. 3, pp. 1278–1319, Mar. 2010, doi: 10.1021/cr800344k.

[55] E. Flores, P. Novák, and E. J. Berg, “In situ and Operando Raman Spectroscopy of Layered Transition Metal Oxides for Li-ion Battery Cathodes,” *Front. Energy Res.*, vol. 6, p. 82, Aug. 2018, doi: 10.3389/fenrg.2018.00082.

[56] S.-W. Song, K.-S. Han, H. Fujita, and M. Yoshimura, “In situ visible Raman spectroscopic study of phase change in LiCoO2 ®lm by laser irradiation,” *Chem. Phys. Lett.*, 2001.

[57] C. Snyder, C. Apblett, A. Grillet, T. Beechem, and D. Duquette, “Measuring Li^+ Inventory Losses in $LiCoO_2$ /Graphite Cells Using Raman Microscopy,” *J. Electrochem. Soc.*, vol. 163, no. 6, pp. A1036–A1041, 2016, doi: 10.1149/2.1111606jes.

[58] T. R. Jow, S. A. Delp, J. L. Allen, J.-P. Jones, and M. C. Smart, “Factors Limiting Li^+ Charge Transfer Kinetics in Li-Ion Batteries,” *J. Electrochem. Soc.*, vol. 165, no. 2, pp. A361–A367, 2018, doi: 10.1149/2.1221802jes.

[59] X.-Y. Qiu *et al.*, “Electrochemical and electronic properties of LiCoO 2 cathode investigated by galvanostatic cycling and EIS,” *Phys. Chem. Chem. Phys.*, vol. 14, no. 8, pp. 2617–2630, 2012, doi: 10.1039/C2CP23626E.

[60] R. Weber, A. J. Louli, K. P. Plucknett, and J. R. Dahn, “Resistance Growth in Lithium-Ion Pouch Cells with $LiNi_{0.80}Co_{0.15}Al_{0.05}O_2$ Positive Electrodes and Proposed Mechanism for Voltage Dependent Charge-Transfer Resistance,” *J. Electrochem. Soc.*, vol. 166, no. 10, pp. A1779–A1784, 2019, doi: 10.1149/2.0361910jes.

[61] M. Sumita and T. Ohno, “Multi-spin-state at a Li_3PO_4/$LiCoO_2$ (104) interface,” *Phys. Chem. Chem. Phys.*, vol. 18, no. 6, pp. 4316–4319, 2016, doi: 10.1039/C5CP07735D.

[62] D. P. Abraham, E. M. Reynolds, E. Sammann, A. N. Jansen, and D. W. Dees, “Aging characteristics of high-power lithium-ion cells with LiNi0.8Co0.15Al0.05O2 and Li4/3Ti5/3O4 electrodes,” *Electrochimica Acta*, vol. 51, no. 3, pp. 502–510, Oct. 2005, doi: 10.1016/j.electacta.2005.05.008.

[63] T. Osaka, S. Nakade, M. Rajamäki, and T. Momma, “Influence of capacity fading on commercial lithium-ion battery impedance,” *J. Power Sources*, vol. 119–121, pp. 929–933, Jun. 2003, doi: 10.1016/S0378-7753(03)00233-7.

[64] H. Zhang *et al.*, “Rock-Salt Growth-Induced (003) Cracking in a Layered Positive Electrode for Li-Ion Batteries,” *ACS Energy Lett.*, vol. 2, no. 11, pp. 2607–2615, Nov. 2017, doi: 10.1021/acsenergylett.7b00907.

[65] N. Iqbal *et al.*, “Effects of Diffusion-Induced Nonlinear Local Volume Change on the Structural Stability of NMC Cathode Materials of Lithium-Ion Batteries,” *Mathematics*, vol. 10, no. 24, Art. no. 24, Jan. 2022, doi: 10.3390/math10244697.

[66] C. Wang *et al.*, “Direct observation of chemomechanical stress-induced phase transformation in high-Ni layered cathodes for lithium-ion batteries,” *Matter*, vol. 6, no. 4, pp. 1265–1277, Apr. 2023, doi: 10.1016/j.matt.2023.02.001.

APPENDIX A: SUPPORTING INFORMATION ON THE CYCLE LIFE STUDIES OF ELECTRODEPOSITED LITHIUM COBALT OXIDE

In Fig. A1, we show the single spectra of LCO at different states of charge. As the voltage increases, The two-mode spectra of LCO transitions into a four mode spectra. The two mode spectra represent the E_g+A_{1g} modes seen for fully lithiated LTMO materials. The presence of the four mode spectra indicates that a given region is in the charged state.

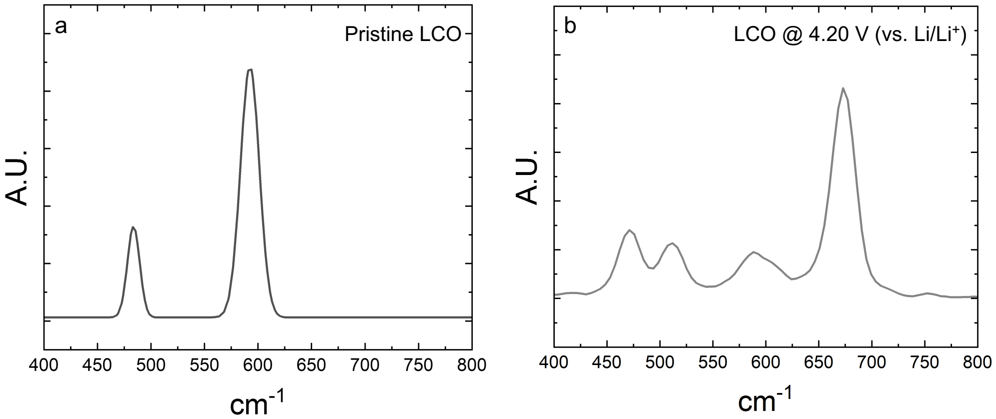

Figure A1: a) Raman spectra of $LiCoO_2$ in the fully discharged state. b) Raman spectra of $LiCoO_2$ in the charged state.

In Fig. A2, postmortem SEM images of each LCO cathode included in this paper are depicted. We see evidence of degradation in each cross-sectioned cathode.

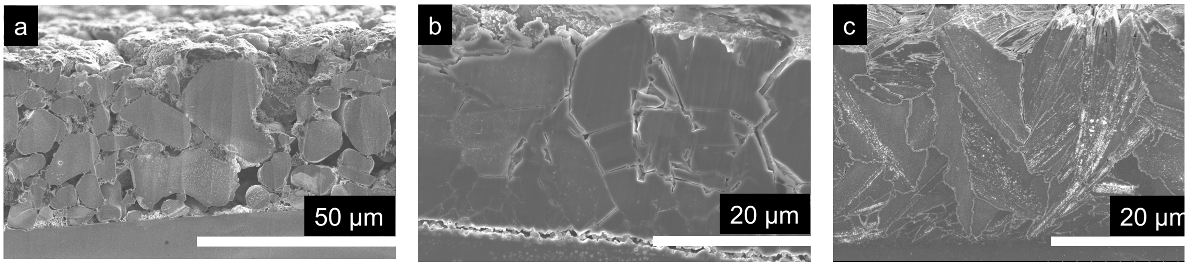

Figure A2: Postmortem SEM images of LCO cathodes. a) Postmortem composite LCO. b) Postmortem (003) LCO. Cracks are seen throughout this cross-section. The electrode appears to have delaminated during cycling. c) Postmortem (104) LCO. Small separation between branches of the electrode are visible.

In Fig. A3, we show a cracked particle in the postmortem A-LCO electrode. This sample was cycled 100 times at a C/2 rate. This image further supports our assertion that individual particles crack during electrochemical cycling. These cracks can isolate regions of single crystals in the cathode and decrease the total active mass of the cathode.

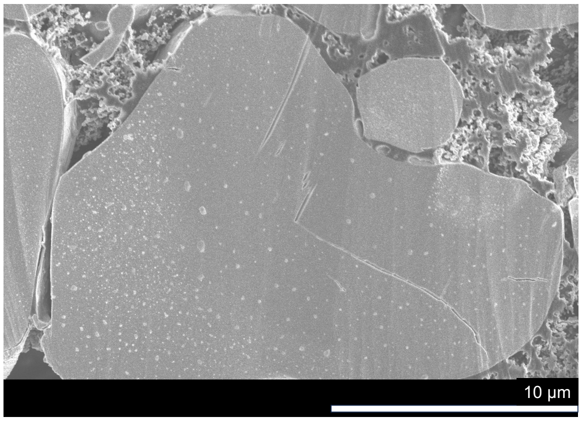

Figure A3: SEM image of postmortem A-LCO.

In Fig. A4, an alternate SEM image of postmortem (003) LCO is provided. This image shows cracks run throughout the structure of this cathode after 100 electrochemical cycles. This image

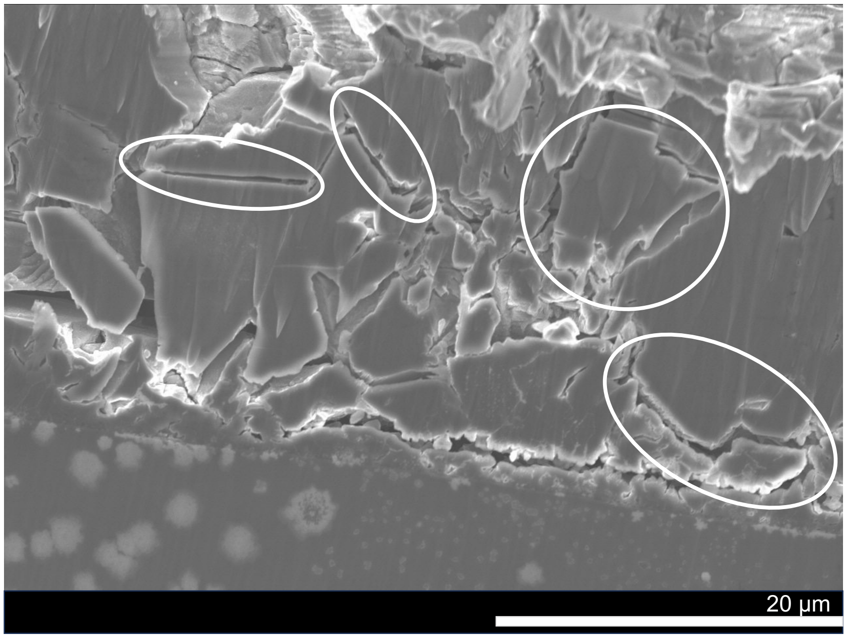

Figure A4: SEM image of postmortem (003) LCO. The circled regions are exemplar areas where cracks appear in the cathode.

supports our assertion that the (003) LCO sample is mechanically inferior to the other films included in this study.

To further support our assertion that (003) textured cathodes are susceptible to crack formation, an additional postmortem Raman image is depicted in Fig. A5. This image shows that the deposited electrode is not only fragile at the substrate but also across the direction parallel to the substrate. Furthermore, we see that these cracked sections isolate functional regions of the film from further electrochemical reaction.

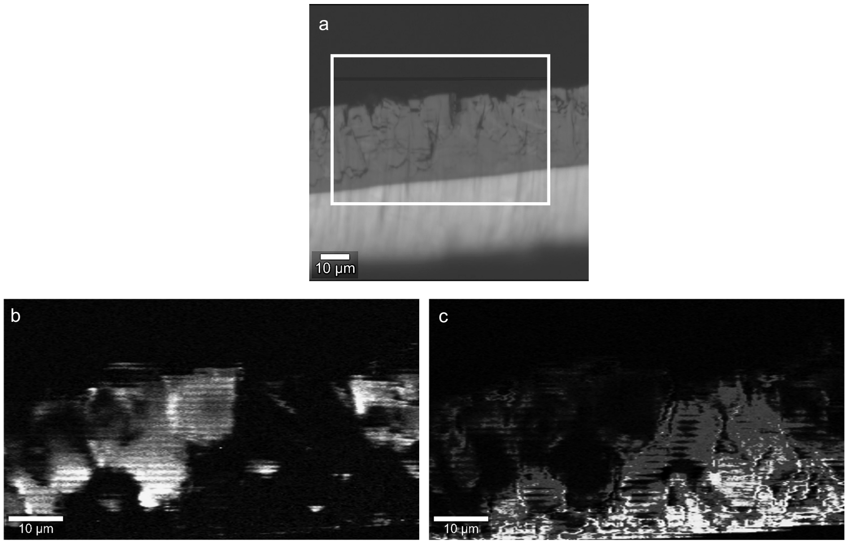

Figure A5: Additional postmortem Raman image of (003) LCO. a) Bright field image of postmortem (003) LCO cross-section. b) Raman image of postmortem (003) LCO cross-section at 590 cm^{-1}. c) Raman image of postmortem (003) LCO cross-section at 670 cm^{-1}.

An alternate SEM image of postmortem (104) LCO in is shown Fig. A6. We see evidence of separation in individual grains of material, but large-scale cracking is not present in this material. An additional postmortem Raman image of (104) LCO is shown in Fig. A7. The bright field image shown in Fig. A7a depicts minimal evidence of cracking in the LCO cross-section. The 590 cm^{-1} image shown in Fig. A7b reveals that a large area of this electrode is still available for electrochemical cycling. The 670 cm^{-1} image reveals that the area surrounding these active regions are lithium deficient and connected to the measured capacity loss for this cathode.

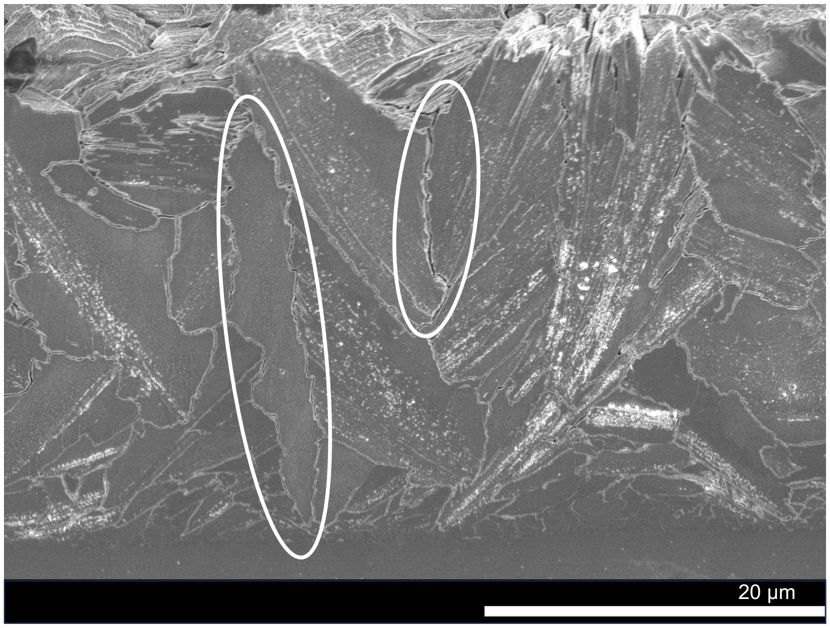

Figure A6: SEM image of postmortem (104) LCO.

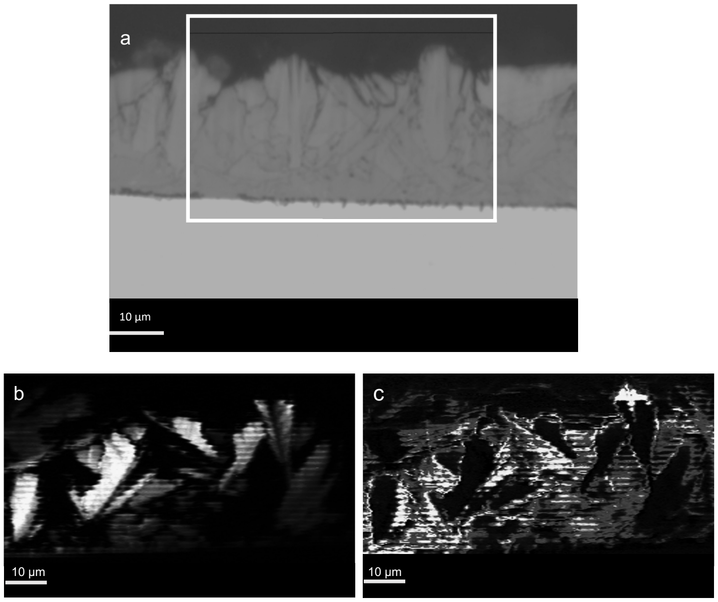

Figure A7: Additional postmortem Raman image of (104) LCO. a) Bright field image of the postmortem (104) LCO cross-section. b) Raman image of postmortem (104) LCO cross-section at 590 cm^{-1}. c) Raman image of postmortem (104) LCO cross-section at 670 cm^{-1}. These images reveal that active branches of (104) LCO are surrounded by high-voltage LCO.

Half-cell characterization for each film included in this study is shown in Fig. A8. In Fig. A8a, we show the first cycle for each film. The similar first cycle coulombic efficiency for each cell makes it apparent that the electrochemical performance of each film is comparable. The rate ladder results obtained for each cathode are plotted in Fig. A8b. For the first five cycles, the discharge C-rate for each cell was C/10. Each of the cathodes maintain their discharge capacity well up to the rate is increased to C/2. At 2C, the discharge capacity of (003) LCO and (104) LCO begin to fade rapidly, possibly due to intercalation induced stress becoming more severe at elevated cycling rates. The capacity retention of these cathodes recovers to >85% when the cycling rate is reduced to C/10. These results indicate that slower rates of cycling alleviate the effect of Li^+ charge transfer kinetics in textured LCO films. Increasing the cycle rate applied to the composite LCO film does not reduce the capacity retention of this film below 85%. This result supports the assertion that the Li^+ charge transfer kinetics are not the dominating factor for capacity fade in A-LCO. We believe that intercalation induced stress at this cycling rate reduces the viability of textured films in comparison to A-LCO for rapid discharge applications. The EIS results at low and high voltage are illustrated in Fig. A8c-e. (003) LCO shows the most dramatic decrease in impedance as the half-cell voltage increases. These EIS results reflect that it is more difficult to remove and insert lithium into (003) LCO at low voltages than it is to exchange lithium into (104) LCO and A-LCO at similar voltages.

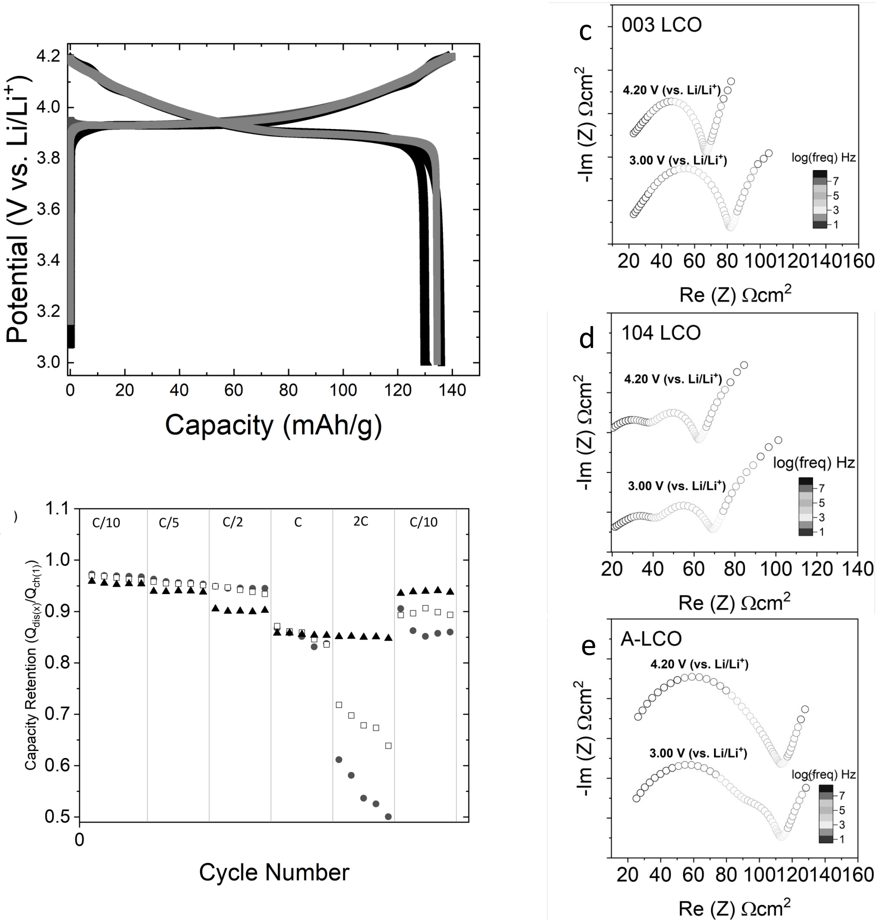

Figure A8: Additional postmortem Raman image of (104) LCO. a) Bright field image of the postmortem (104) LCO cross-section. b) Raman image of postmortem (104) LCO cross-section at 590 cm^{-1}. c) Raman image of postmortem (104) LCO cross-section at 670 cm^{-1}. These images reveal that active branches of (104) LCO are surrounded by high-voltage LCO.

We include an example of the fitted EIS spectra in Figure A9. The simplex method was applied to the raw data to minimize the fitting error. This process was repeated for all collected spectra.

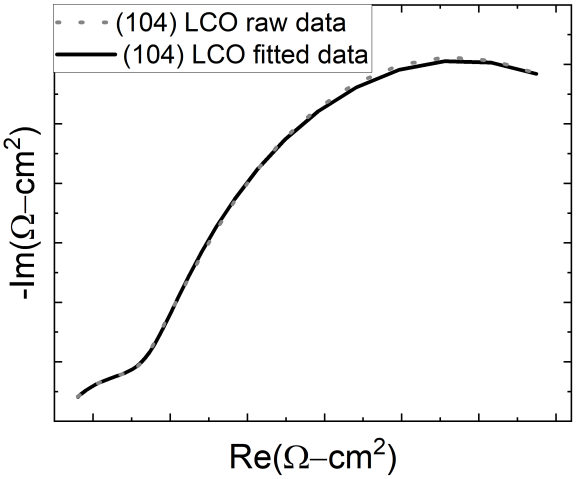

Figure A9: Fitted EIS result for (104) LCO. The raw EIS data was fitted using the simplex method to obtain accurate numbers to describe the electrochemical behavior of this cathode.

The cathodes used in the postmortem Raman images were cycled in full cells. The electrochemical data for these cells is shown in Figure A10. (104) LCO displays the best cycling performance, retaining 71.3% of its available capacity after 100 cycles at C/2. On the other hand (003) LCO and A-LCO retain 42.2% and 67.9% of their available capacity, respectively.

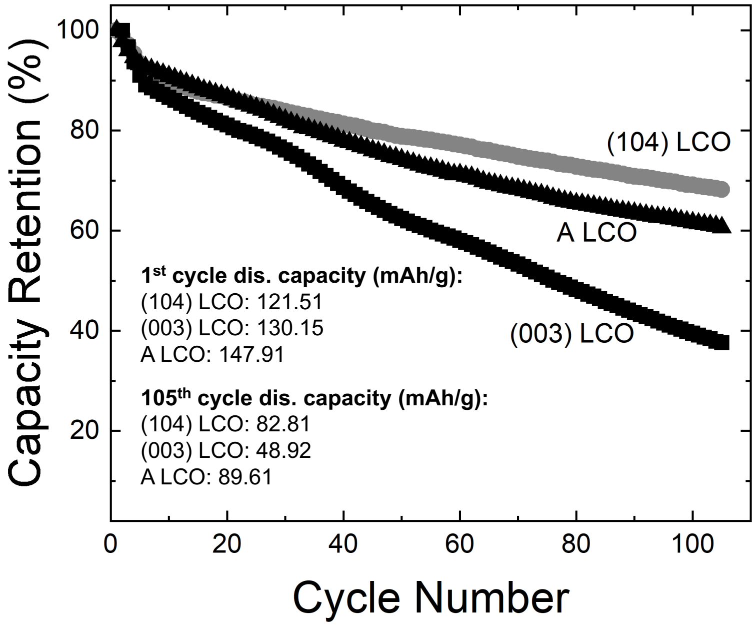

Figure A10: Full cell capacity retention vs. cycle number. Each film was cycled against a graphite counter electrode at C/2 for 100 cycles.

The EIS spectra of cathodes cycled in full cells is depicted in Figure A11. A-LCO experiences the largest growth in R_{CEI}. This CEI is an additional barrier for lithium-ion diffusion. R_{CT} of textured electrodes grows rapidly during the cycle life of each cathode. The limited electroactive surface area remaining appears to be compensated when reducing the cell cycling rate as capacity can be recovered for textured electrodes under these conditions.

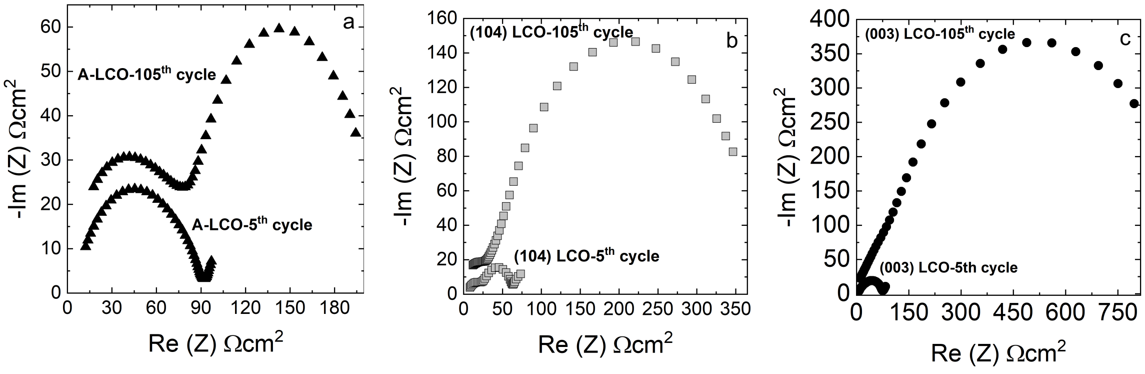

Figure A11: EIS summary of LCO electrodes in the discharged state (3.00 V vs. Li/Li$^+$) at the beginning and end of the cycle life. a) A-LCO EIS summary. b) (104) LCO EIS summary. c) (003) LCO EIS summary.